2007

A DUAL FREQUENCY TRANSMITTER FOR ENHANCED POLAR OUTFLOW PROBE(e-POP) MISSION

Guowei Li
Western University

A DUAL FREQUENCY TRANSMITTER FOR ENHANCED *POLAR OUTFLOW PROBE(e-POP)* MISSION

(Spine title: A Dual Frequency Transmitter For e-POP Mission)

(Thesis format: Monograph)

by

Guowei Li

Graduate Program in Engineering Science
Department of Electrical and Computer Engineering

Submitted in partial fulfillment
of the requirements for the degree of
Master of Engineering Science

Faculty of Graduate Studies
The University of Western Ontario
London, Ontario
October, 2007

ABSTRACT

In 2008, a satellite named CASSIOPE (Cascade SmallSat and Ionospheric Polar Explorer) will be launched. The e-POP (Enhanced Polar Outflow Probe) payload on it will be used to conduct research on the ionosphere. A HF Tomography technique, which needs HF signals transmitted from ground-based transmitters and collected by the e-POP, is proposed to generate the ionospheric tomographic reconstruction images. According to the technique, the transmitters are required to transmit two pulsed adjacent frequency signals in the HF band and work synchronously with each other. A new dual-frequency transmitter has been developed for this purpose. In each transmitter, a 16-bit microcontroller can control DDS chips to generate two pulsed closely spaced frequency signals and it allows users to set up parameters through input switch panels. Several coding methods, such as Barker and Legendre, can be chosen for modulation. GPS system and Time Division Multiple Access (TDMA) scheme are applied to synchronize and accommodate transmitters in different locations. Lab and field experiments have demonstrated that the transmitter can satisfy the requirements of the HF Tomography technique for the e-POP mission. A network of three of these transmitters also operates with a CADI receiver to measure the TIDs in the ionosphere. Observation results are shown and compared with those from other researchers.

Keywords: HF Tomography, e-POP, HF Transmitter, TID

ACKNOWLEDGEMENTS

I would like to extend my deepest appreciation to my supervisor, Prof. John. W. MacDougall for his patient guidance of my thesis project, and his kindness, understanding, and encouragement.

Thanks go to Jing Huang and Lan Wang for their helps through my projects. I would also like to thank staffs in Electronic shop of Electrical Engineering Department, and Doug Hie, Phin Perquin, and Brian Dalrymple in Physics Department for their supports.

Special thanks to my parents for their constant moral support.

TABLE OF CONTENTS

CERTIFICATE OF EXAMINATION II

ABSTRACT III

ACKNOWLEDGEMENTS IV

TABLE OF CONTENTS V

LIST OF TABLES VIII

LIST OF FIGURES IX

Chapter 1. Introduction 1

1.1 Ionosphere 1

1.2 Enhanced Polar Outflow Probe Satellite(e-POP) 1

1.3 Overview of the Project 4

Chapter 2. Ionospheric Radio Propagation and Probing 5

2.1 Radio Propagation in Ionosphere 5

2.1.1 Plasma Frequency 5

2.1.2 Gyro-frequency 5

2.1.3 Refractive Index Noise 6

2.1.4 Snell's Law of Refraction 7

2.1.5 Group Velocity v_g 8

2.1.6 Radio Wave Propagation and Virtual Height 8

2.2 Acoustic-gravity Waves and Traveling Ionosphere Disturbances (TIDs) 10

2.2.1 Acoustic-gravity Waves 10

2.2.2 Traveling Ionosphere Disturbances 11

2.2.3 Measurement of TIDs 12

Chapter 3. RADAR Principles and CADI System 15

3.1 Radar Principles 15

3.1.1 Range Detection 15

3.1.2 Range Resolution 16

3.1.3 Radar Equation 17

3.1.4 Pulse Compression 19

3.2 The CADI System 22

3.2.1 Overview of the CADI System 22

3.2.2 Operation Modes 25

3.2.3 Signal Processing in the Receiving Board 25

Chapter 4. Design of the New Transmitter 27

4.1 Requirements 27

4.2 Overview of the Transmitter 28

4.3 GPS 29

4.4 DDS Board 30

4.4.1 Input Panel 30

4.4.2 Microcontroller 32

4.4.3 DDS Chip 36

4.4.4 Low Pass Filter 41

4.4.5 RF Switch 42

4.4.6 Power Combiner 43

4.4.7 Small Signal Amplifier 44

4.5 Pre-Amplifier 44

4.6 Power Amplifier 45

4.7 Performance of the Transmitter 46

Chapter 5. The Experimental Setup and Results 51

5.1 Experimental Setup 51

5.2 Lab Experiments 53

5.3 Field Experiments 54
5.3.1 Data Analysis 54
5.3.2 TIDs Analysis 57
5.3.3 Results 59

Chapter 6. Conclusion and Recommendations 72

6.1 Conclusion 72
6.2 Recommendations 73
6.2.1 The Oscillator 73
6.2.2 The pre-Amplifier 74
6.2.3 Observations of TIDs 74

APPENDICES 76

REFERENCE 77

VITA 80

LIST OF TABLES

Table 3-1 Characteristics of several codes 23

Table 3-2 Specifications of CADI system 23

Table 4-1 Configuration of 9S12 microcontroller ports 33

LIST OF FIGURES

Figure 1.1 Typical Vertical Profiles of Electron Density 2

Figure 1.2 Coordinated operations between CASSIOPE/e-POP satellite and ground radar facilities 3

Figure 2.1 Refraction of a radio wave in a horizontal stratified ionosphere 7

Figure 2.2 True and virtual height of radio propagation in ionosphere 9

Figure 2.3 Virtual height variations of ordinary ray at 5.8 Mc./sec on 5 July 1948..... 12

Figure 2.4 Measurement of a TID Wave 13

Figure 3.1 The basic principle of range measurement in a pulsed radar system 16

Figure 3.2 Illustration of the range resolution 18

Figure 3.3 Diagram of binary phase coding system 20

Figure 3.4 Autocorrelation function of Barker 13 20

Figure 3.5 Diagram of CADI 24

Figure 4.1 Time schedule for a 5-transmitter ionospheric tomography system 28

Figure 4.2 Diagram of transmitter 28

Figure 4.3 Block diagram of DDS board 30

Figure 4.4 Schematic of the DDS Board 31

Figure 4.5 Flowchart of microcontroller main program 34

Figure 4.6 Flowchart of the microcontroller ISR routine 35

Figure 4.7 Sampled amplitude and phase of a sine wave 37

Figure 4.8 Block diagram of AD9851 39

Figure 4.9 AD9851 output spectrum of a sample wave at 20MHz 40

Figure 4.10 AD9851 parallel frequency upload timing sequence 41

Figure 4.11 Performance of ADG751BRM 43

Figure 4.12 Spectrum of the output of PSC-2-1 with two inputs: 18MHz and 17.985MHz 44

Figure 4.13 Schematic of the power amplifier 45

Figure 4.14 5-element Chebyshev low-pass filter 46

Figure 4.15 Attenuation response curve of the Chebyshev low-pass filter 47

Figure 4.16 Power amplifier output of an 18MHz sine wave 48

Figure 4.17 Power amplifier output of 18MHz and 17.985MHz sine waves 48

Figure 4.18 Power amplifier output power versus frequency 50

Figure 5.1 Locations of the field experimental transmitters and receiver setup 51

Figure 5.2 Timing diagram of the field experiment system 53

Figure 5.3 Transmitter synchronization experiments results 55

Figure 5.4 User interface of the data analysis Matlab program 56

Figure 5.5 User interface for TIDs analysis 57

Figure 5.6 Different TIDs shapes on h't plot 58

Figure 5.7 *h't* plots from field experiment on July 15th, 2007 60

Figure 5.8 Observation of X and Loop type disturbances at hour 11, August 25 62

Figure 5.9 Observation of Y type disturbances at hour 0, August 17 62

Figure 5.10 Observation of Z type disturbances at hour 17, August 22 63

Figure 5.11 Observation of peaks and dips at hour 15, August 17 63

Figure 5.12 Observations of abrupt changes at hour 11-12, August 21 64

Figure 5.13 Observations of crossover at hour 23, August 18 64

Figure 5.14 Occurrences distribution of TIDs over time.....66

Figure 5.15 TIDs speed and direction distribution over time.....66

Figure 5.16 TIDs moving direction distribution.....67

Figure 5.17 TIDs moving speed distribution.....68

Figure 5.18 Comparison of TIDs speed distribution between daytime and nighttime...69

Figure 5.19 Comparison of TIDs direction distribution between daytime and nighttime 70

Chapter 1. Introduction

1.1 Ionosphere

The Ionosphere is the region of the atmosphere lying between approximately 50 km and 1000 km. Most of the ionosphere is electrically neutral, but when solar radiation strikes the chemical constituents of the atmosphere, molecules are ionized to produce the ionospheric plasma. Although the charged particles are only a minority amongst the neutral ones, it is their presence that makes the upper atmosphere an electrical conductor and brings about the possibility of radio communication over large distances.

The ionosphere has historically been divided into three regions: D, E, and F, primarily, by height [Davis, 1968]. The lowest is the D-region which is between about 50 and 90 km. The electron density of this region is around $10^9/m^3$ during day time, and free electrons almost disappear at night time. The E-region lies between 90 and 140 km and is divided into two layers: the normal E layer and sporadic layers, Es. The electron density is in the order of $10^{11}/m^3$ during day time and drops down to $10^{10}/m^3$ at night time. The F-region is the ionosphere above the E-region. Within the F-region are the F1 and F2 layers. The electron density may reach $10^{12}/m^3$ in day time and $6\times10^{10}/m^3$ at night time. Figure 1.1 shows electron-density profiles of the ionosphere.

1.2 Enhanced Polar Outflow Probe Satellite(e-POP)

In 2008, a satellite named CASSIOPE (Cascade SmallSat and Ionospheric Polar Explorer), entirely designed and built in Canada, will be launched. "CASSIOPE is a new generation of small-satellite and multifunctional platform technology demonstration

program of CSA (Canadian Space Agency) with the goal to serve both, namely scientific and commercial support applications in a variety of future Canadian space missions." [EOPORTAL, 2006]

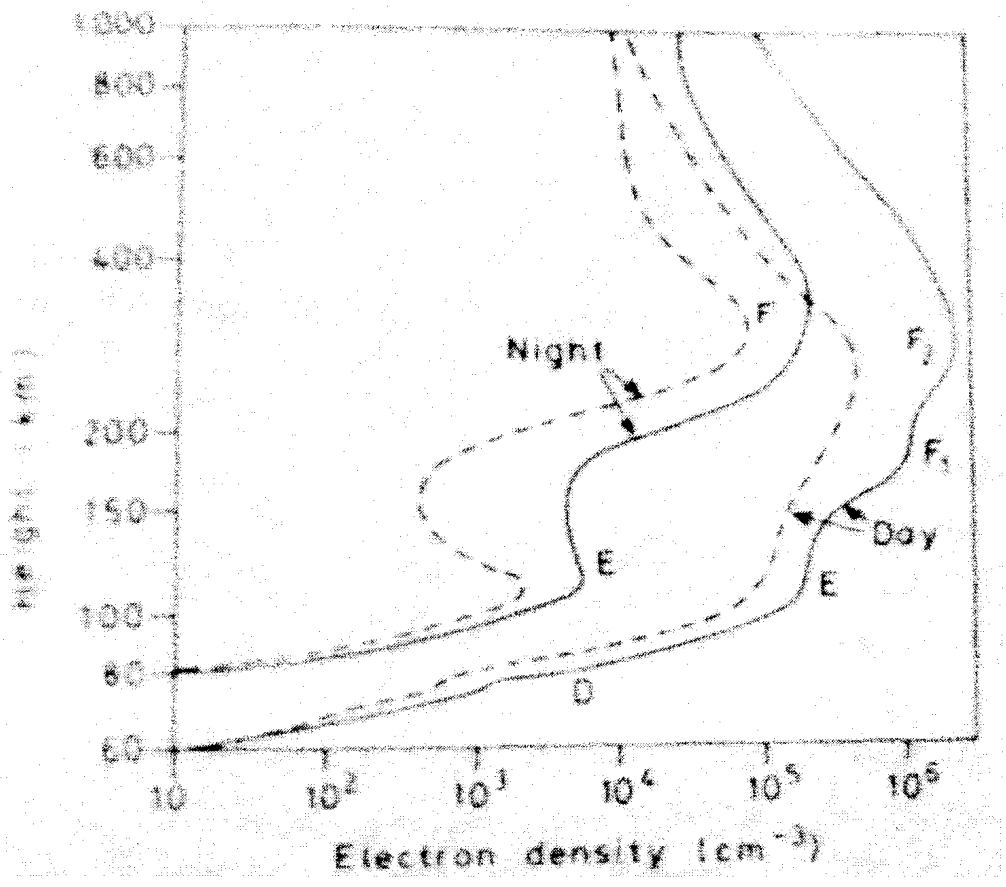

Figure 1.1 Typical vertical profiles of electron density [Hunsucker, 2003] Dashed line: sunspot minimum; Solid line: sunspot maximum

A payload, e-POP (Enhanced Polar Outflow Probe), is carried on the satellite to conduct research on the ionosphere. The e-POP probe will study space weather phenomena in the Earth's upper atmosphere, where the solar wind interacts with the magnetic field of the earth. It will help scientists have a better understanding of solar storms and their impacts on space technologies such as those used in radio communications and GPS navigation. The e-POP project team is led by Dr. Andrew Yau from the Institute for Space Research at the University of Calgary and is composed of

scientists and engineers from seven Canadian universities and three research organization. The planned orbit of e-POP is an inclined elliptical orbit. Its apogee and perigee are at 1,500 km and 300 km respectively. The planned initial inclination is approximately 80 degrees.

The e-POP probe includes eight scientific instruments. One of them is a radio receiver instrument, called RRI. In the HF band, RRI will conduct a classical transionosphere propagation study, in conjunction with the Canadian Advanced Digital Ionosonde (CADI) and the Super Dual Auroral Radar Network (SuperDARN) transmitters on the ground. As shown in Figure 1.2, RRI will collect HF signals sent by ground based radars and bent by plasma irregularities. The measurements will include the signal amplitude, group delay, and direction of arrival [Liu, W., et al, 2004].

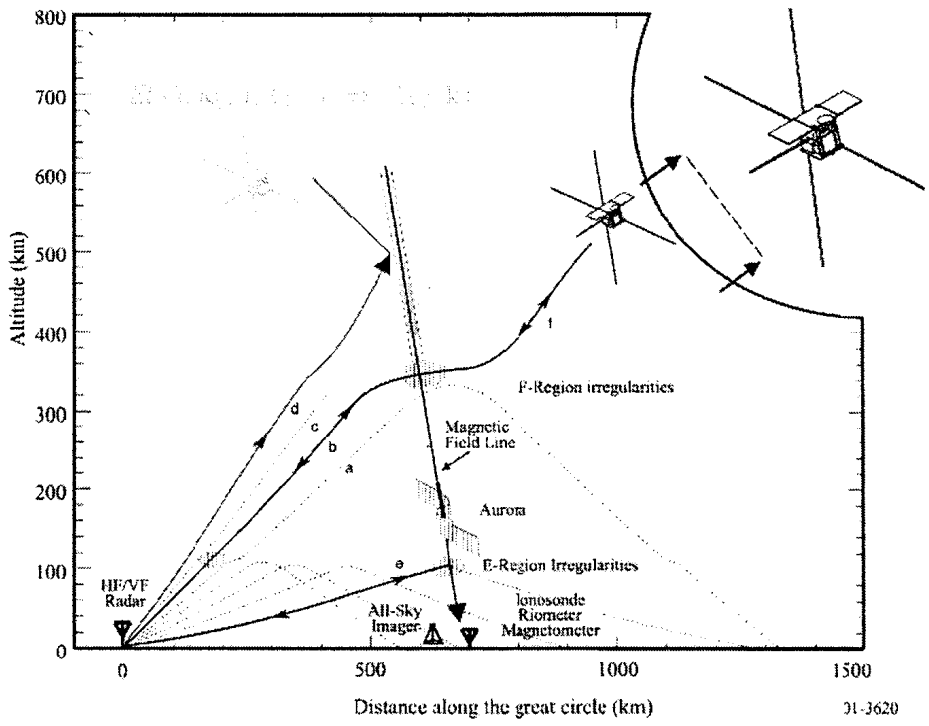

Figure 1.2 Coordinated operations between CASSIOPE/e-POP satellite and ground radar facilities

1.3 Overview of the Project

In her thesis, Wang [2006] presented the HF Tomography technique. In this algorithm, HF signals that are sent out from ground-based transmitters and collected by satellites are used to generate the ionospheric tomographic reconstruction images, which illustrate height versus geographic latitude electron density distributions. Theoretical simulations have demonstrated its capabilities in mapping and modeling the ionized atmosphere [Wang, 2006]. The launch of e-POP will provide a chance to investigate and verify this idea.

According to the requirement of the HF Tomography, a schematic of a new transmitter has been proposed. In the future, several of these transmitters will be deployed. RRI on e-POP will collect the HF signals sent from these transmitters. The data will then be used to demonstrate the HF Tomography and support other studies e-POP is supposed to make.

My objective is to design, develop, and test this transmitter. In order to assess its performance, it is tested with a CADI radar system to measure the ionosphere and do studies of traveling ionospheric disturbances (TIDs).

In this thesis, Chapter one introduces the ionosphere, discusses the e-POP mission, and describes the motivation of this project. Basic theories of ionospheric radio propagation, gravity waves, and TIDs are introduced in Chapter two. Chapter three includes some radar principles and illustration of the CADI system. A detailed description of the new transmitter and its development is given in Chapter four. The experimental setup and results are examined in Chapter five. The final chapter presents conclusions and recommendations for future work.

Chapter 2. Ionospheric Radio Propagation and Probing

2.1 Radio Propagation in Ionosphere

2.1.1 Plasma Frequency

The ionosphere can be considered as a cold weakly ionized gas (plasma) with the Earth's magnetic field superposed. The plasma frequency f_N is the natural frequency of oscillation of the free electrons which have been displaced from the heavy positive ions and are allowed to move freely thereafter [Davies, 1969]. It is given as:

$$f_N^{\,2} = \frac{Ne^2}{4\pi^2 \varepsilon_0 m} \tag{2.1}$$

where N is electron density (electrons per m^3), ε_0 is permittivity of free space (8.85×10^{-12}F/m), e is charge of an electron (1.6×10^{-19} coulombs), and m is rest mass of electron (9.1×10^{-31} Kg). Obviously, the plasma frequency increases with the electron density.

For waves propagating vertically into the ionosphere, the maximum plasma frequency of a layer is usually called critical frequency. The wave with frequency at or below it is reflected, and wave with frequency above it penetrates through the layer

2.1.2 Gyro-frequency

In the external magnetic field $\boldsymbol{B}$, electrons or ions in the ionosphere will spirally gyrate around $\boldsymbol{B}$ at a certain frequency. This frequency is called gyro-frequency, f_H , and is defined as:

$$f_H = \frac{|e|}{2\pi m} B \tag{2.2}$$

where m is the mass of the particle, and $|e|$ is the charge.

2.1.3 Refractive Index

In a neutral medium with a uniform external magnetic field, the complex refractive index, *n*, of a radio wave is given by the Appleton formula [Davies, 1990]:

$$n^2 = (\mu - i\chi)^2 = 1 - \frac{X}{1 - iZ - \frac{Y_T^2}{2(1 - X - iZ)} \pm \left[\frac{Y_T^4}{4(1 - X - iZ)} + Y_L^2 \right]^{1/2}} \tag{2.3}$$

where $X = (f_N / f)^2$, $Y = f_H / f$, $Y_L = Y \cos\theta$, $Y_T = \sin\theta$, $Z = \upsilon / f$, χ is the absorption coefficient, υ is the electron collision frequency, and θ is the angle between the magnetic field and the direction of phase propagation. Y_L and Y_T are the longitudinal and transverse components of gyro-frequency respectively.

In the absence of the magnetic field, $Y_L = Y_T = 0$. The refractive index is:

$$n^2 = 1 - \frac{X}{1 - iZ} \tag{2.4}$$

In the E and F regions, the electron collision frequency is very low and can be neglected. Then (2.3) becomes:

$$\mu^2 = 1 - \frac{2X(1 - X)}{2(1 - X) - Y_T^2 \pm \left[Y_T^4 + 4(1 - X)^2 Y_L^2 \right]^{1/2}} \tag{2.5}$$

Reflection conditions for vertical propagation can be found by setting $\mu = 0$ in (2.5). The positive sign gives

$$X = 1 \tag{2.6}$$

and the negative sign gives

$$X = 1 - Y \text{ or } X = 1 + Y \tag{2.7}$$

Waves with positive sign are usually called the 'ordinary' waves since they are reflected at the same height as they would be in the absence of the magnetic field. The

waves with the negative sign are called extraordinary waves, among which the wave with $X = 1 + Y$ is also called the z-wave. Ordinary and extraordinary waves have different polarization. Normally, extraordinary waves have higher critical frequency than ordinary waves.

In the ionosphere, when both magnetic field effects and collisions are negligible, the refractive index can be represented as:

$$\mu = \sqrt{1 - \left(\frac{f_N}{f}\right)^2} \tag{2.8}$$

where f_N is the plasma frequency and f is the radio wave frequency.

2.1.4 Snell's Law of Refraction

Consider an ideal horizontally stratified ionosphere as illustrated in Figure 2.1. A radio wave is incident on the ionosphere with angle ϕ_0.Snell's law indicates that

$$\mu_0 \sin\phi_0 = \mu \sin\phi = u_r \sin\phi_r \tag{2.9}$$

The wave is reflected when angle $\phi_r = 90^0$. For simplicity, suppose $\mu_0 = 1$.Then the refractive index required for reflection is given by:

$$\mu_r = \sin\phi_0 \tag{2.10}$$

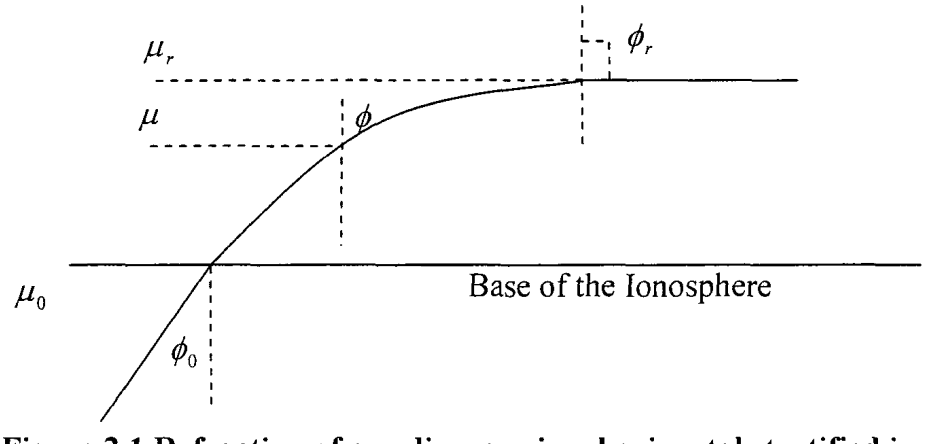

Figure 2.1 Refraction of a radio wave in a horizontal stratified ionosphere

2.1.5 Group Velocity v_g

When a wave travels through the ionosphere, in which both magnetic field effects and collisions are negligible, its group velocity v_g can be written as:

$$v_g = c\sqrt{1-\frac{f_N^2}{f^2}} \tag{2.11}$$

This equation shows that group velocity decreases while plasma frequency increases. From equation (2.1), we know that plasma frequency increases with electron density. So, if a wave travels through a medium where electron distribution grows denser, its group velocity keeps decreasing.

2.1.6 Radio Wave Propagation and Virtual Height

Suppose a radio wave penetrates into the ionosphere vertically and is reflected to the ground. From equation (2.10), this wave is reflected at a place where the refractive index is 0. According to equation (2.8) and (2.11), this means that the wave is reflected when its group velocity decreases to 0.

As illustrated in Chapter 1, the electron density, and therefore the plasma frequency, in the ionosphere normally increases with the altitude and has two main peaks in E and F region respectively. If a wave penetrates vertically into the ionosphere and its frequency is higher than the maximum plasma frequency, its group velocity will not decrease to 0, and then the wave will not be reflected.

On the contrary, if its frequency is lower than the maximum plasma frequency, its group velocity will decrease towards 0 until it is reflected. The altitude of the reflection point is called the true height. If the flight time of this wave, t, is measured, with the assumption that the radio wave travels with the velocity of light, c, the virtual height of

the reflection point is given as:

$$H_v = \frac{1}{2}ct \tag{2.12}$$

As this wave travels at group velocity which decreases from velocity of light to 0, the virtual height is higher than the true height. This is shown in Figure 2.2.

If a wave penetrates into the ionosphere obliquely and is reflected back to ground, its true height and virtual height are also illustrated in Figure 2.2. The relation between the frequency of this wave, f_o, and the frequency of vertically reflected wave at the same true height, f_v,is given as:

$$f_o = f_v \sec\theta_0 \tag{2.13}$$

The frequency, f_v, is called the equivalent vertical frequency. This equation shows that the ionosphere can reflect much higher frequencies with oblique propagation than with vertical propagation.

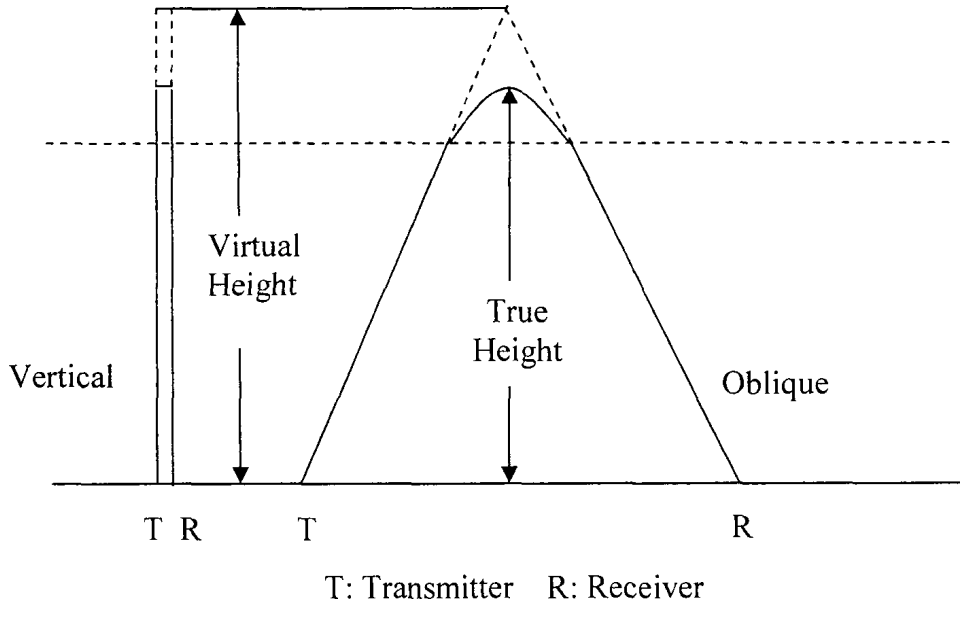

Figure 2.2 True and virtual height of radio propagation in ionosphere

2.2 Acoustic-gravity Waves and Traveling Ionosphere Disturbances (TIDs)

2.2.1 Acoustic-gravity Waves [Davis, 1990]

Consider a plane-stratified, isothermal atmosphere under gravity that is constant with height. If this atmosphere were compressed and then released, it would oscillate around its equilibrium state. The oscillation frequency is called the acoustic-cutoff frequency, ω_a:

$$\omega_a = \frac{C}{2H_s} \tag{2.14}$$

where C is the sound speed, and H_s is the scale height.

Next consider a parcel of gas in the same atmosphere. If this parcel is displaced vertically from its equilibrium, the oscillation frequency is called buoyancy frequency, ω_g:

$$\omega_g^2 = \frac{g}{H_s}\frac{\gamma - 1}{\gamma} \tag{2.15}$$

where g is the gravitational acceleration, and γ is the ratio of the specific heats at constant pressure and constant volume.

Suppose a wave travels in this atmosphere, at an angle ϕ with the vertical, the refractive index is given by

$$\mu^2 = \frac{1 - X_a}{1 - Y_g^{\,2}\sin^2\phi} \tag{2.16}$$

where ω is the frequency of the wave and

$$X_a = (\omega_a/\omega)^2 \tag{2.17}$$

$$Y_g = \omega_g/\omega \tag{2.18}$$

From equation (2.16), we know that the propagation is dispersive and anisotropic. We can also conclude that only two kinds of waves can propagate: one is acoustic waves for frequencies greater than the acoustic-cutoff frequency; the other is the gravity waves for frequencies lower than the buoyancy frequency. The dispersion relation is given as:

$$\omega^4 - \omega^2\omega_a^2 - k_x^2C^2(\omega^2 - \omega_g^2) - C^2\omega^2k_z^2 = 0 \qquad \textbf{(2.19)}$$

where k_x and k_z are the horizontal and vertical component respectively. The ratio of the horizontal displacement ξ of an air parcel to its vertical displacement ζ is

$$\frac{\xi}{\zeta} = -\frac{\mu\sin\phi}{\mu^2\sin^2\phi - 1}\left[\mu\cos\phi - i(X - Y^2)^{1/2}\right] \qquad \textbf{(2.20)}$$

This equation shows that the motions of the air parcel are ellipses in the plane of propagation, and this motion has components transverse to the direction of wave propagation.

2.2.2 Traveling Ionosphere Disturbances [Davis, 1990]

A common feature of the F region ionosphere is the existence of TIDs, which are relatively large-scale, wavelike structures that travel with speeds from 50 m/s to 1000 m/s and periods from a few minutes to more than an hour. TIDs can be divided into two classes: very-large-scale and medium-scale disturbances. Very-large-scale disturbances have wavelengths of the order of 1000 km and periods of 1 hour or more. Medium-scale disturbances usually have wavelengths of the order of 100 to 200 km and periods of 5 to 45 minutes. The medium-scale TIDs are present in the F region about 30-50% of the time, whereas the very-large-scale TIDs are much rarer [Francis, 1974].

As for the origin of TIDs, various suggestions have been made. The most popular one is the acoustic-gravity wave. As Francis states in his paper, '... the hypothesis that TIDs

are ionospheric manifestations of gravity waves, with the ionosphere acting principally as a passive tracer to display the motions of neutral atmosphere, has since received nearly complete acceptance.'[Francis,1975]

2.2.3 Measurement of TIDs

As a way to study acoustic-gravity waves, observations of TIDs have been done by a variety of radar techniques, such as fixed-frequency radar networks [Munro,1958], ionosondes [MacDougall,1997], and multi-frequency HF Doppler radar systems [Georges, 1968]. In this project, as Munro [1958] did, three fixed-frequency transmitters are implemented to observe the horizontal movements of TIDs.

Figure 2.3 shows observations of virtual height of the F region versus time [Munro, 1950]. The most obvious feature of the TIDs is the change in the virtual height. This result shows that the same variation is observed at three places. By measuring the time delay between them, the speed and direction of the TIDs horizontal movement can be determined.

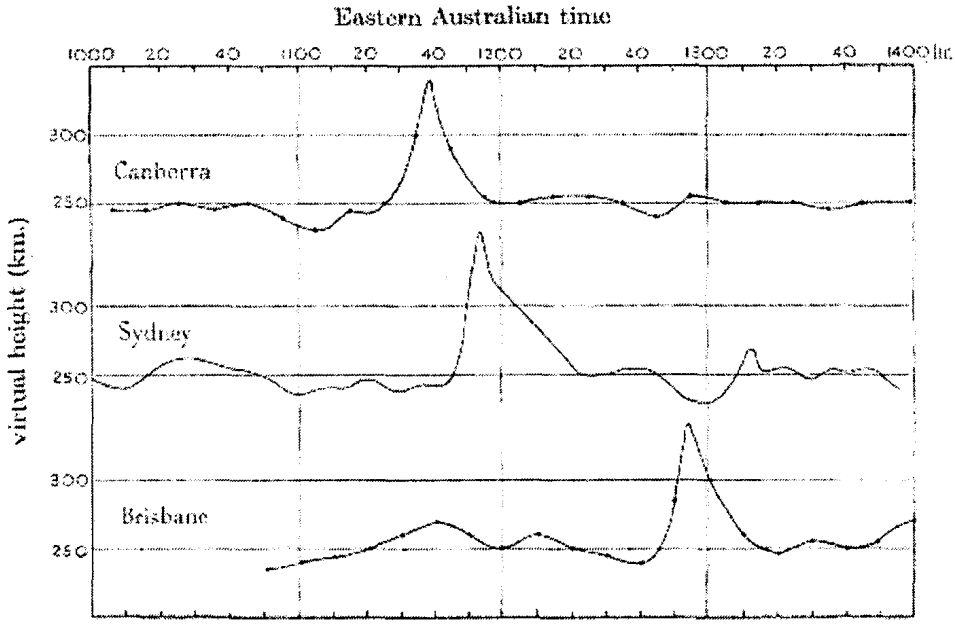

Figure 2.3 Virtual height variations of ordinary ray at 5.8 Mc./sec. on 5 July 1948

Suppose a TID travel in the ionosphere at the speed, V, as shown in Figure 2.4. It is observed at three locations, **A**, **B**, **C** and its direction is represented by $\vec{V}$. Consider a coordination system with origin point at **A**, x axis from **A** to **C**, and y axis pointing to **B**. The distances between **AB** and **AC** are d_{ab} and d_{ac} respectively. τ_{ab} is the time lag between the same observations at **A** and **B**. τ_{ac} is the time lag between the same observations at **A** and **C**. If the TID travels from **A** to **B**, τ_{ab} is positive, otherwise it is negative. If the TID travels from **A** to **C**, τ_{ab} is positive, otherwise it is negative. If the wave travels with angle, θ, clockwise from x axis, we have:

$$d_{ab}\cos(\theta - \phi_{ab}) = V\tau_{ab} \tag{2.21}$$

$$d_{ac}\cos(\theta) = V\tau_{ac} \tag{2.22}$$

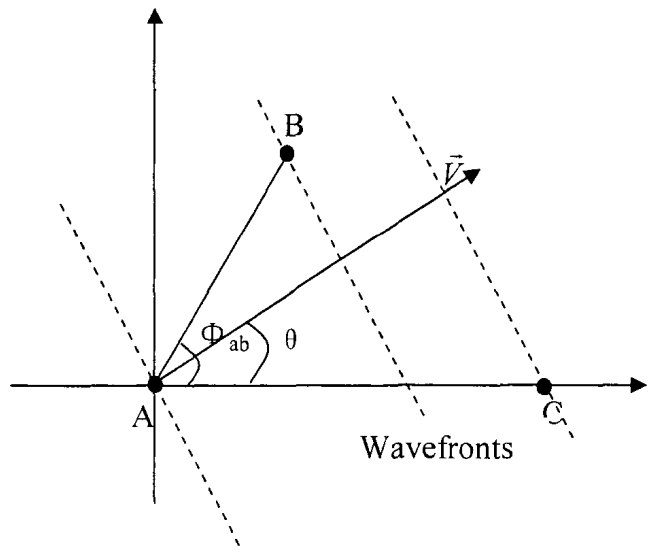

Figure 2.4 Measurement of a TID Wave

From these two equations, the direction of the wave can be obtained:

$$\theta = \arctan\left(\frac{d_{ac}\tau_{ab} - d_{ab}\tau_{ac}\cos\phi_{ab}}{d_{ab}\tau_{ac}\sin\phi_{ab}}\right) \tag{2.23}$$

where $\theta \in (-90^o, 90^o)$. If the wave goes from **C** to **A**, in which case τ_{ac} is negative, the angle $\theta \in (90^o, 270^o)$ is:

$$\theta = 180^0 + \arctan\left(\frac{d_{ac}\tau_{ab} - d_{ab}\tau_{ac}\cos\phi_{ab}}{d_{ab}\tau_{ac}\sin\phi_{ab}}\right) \qquad \textbf{(2.24)}$$

Using the θ from equation (2.23) or (2.24) in equation (2.22), the speed can be obtained.

Chapter 3. RADAR Principles and CADI System

RADAR is the abbreviation of **RA**dio **D**etection **A**nd **R**anging. The basic idea is to use reflected radio waves to detect the appearance and the range of objects. As the proposed transmitter should transmit pulses, this chapter will review some important pulsed radar design considerations and illustrate the CADI radar system.

3.1 Radar Principles

3.1.1 Range Detection

When a pulsed radar detects a target, the target's range, d, is computed by measuring the time delay, Δt. Suppose that the transmitter is in the same place as the receiver. It takes Δt for a pulse to travel the two-way path between the radar and target. Then the target's range would be

$$d = \frac{c \times \Delta t}{2} \tag{3.1}$$

where c is the velocity of electromagnetic wave in the free-space (3×10^8 m/s).

In general, a pulsed radar transmits and receives a train of pulses. As shown in Figure 3.1, it is desirable to receive an echo of a pulse before the next pulse is emitted. Therefore, the relation between the maximum range of interest, d_{max}, and the *pulse repeat interval* (PRI), T_p is

$$d_{\max} = \frac{c \times T_p}{2} \tag{3.2}$$

In order to avoid range ambiguities, PRI should be long enough so that d_{max}>any expected echo distances.

From above, we know that the measurement of range is actually the measurement

of flight time of the pulse, with the assumption that the pulse travels at the velocity of light. If a radar is used to detect the ionosphere, and the transmitter and receiver are located in the same place, the wave will penetrate into the ionosphere vertically. As elaborated in chapter 2, the measurement of range is actually the measurement of virtual height. If the transmitter and receiver are deployed at different locations, the wave will penetrate into the ionosphere obliquely. From figure 2.2, the measurement of range is the measurement of the length of half of the virtual traveling path. Suppose the distance between transmitter and receiver is R, the virtual height is given as:

$$H_v = \sqrt{d^2 - (R/2)^2} \tag{3.3}$$

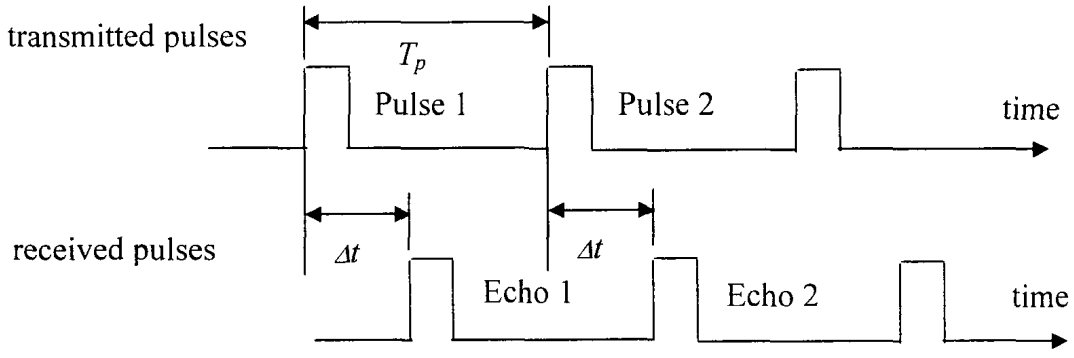

Figure 3.1 The basic principle of range measurement in a pulsed radar system

3.1.2 Range Resolution

Range resolution, ΔR, describes a radar's ability to detect targets very close to each other. It is the smallest distance between two targets that can be resolved in range. Consider two targets located at ranges R1 and R2, as illustrated in Figure 3.2. The width of the transmitted pulse is τ. If the distance between these two targets, b, is greater or equal to $c\tau/2$, they can be resolved. If they are separated by less than $c\tau/2$, they can not be resolved. So, we have

$$\Delta R = \frac{1}{2} c\tau \tag{3.4}$$

As τ is equal to 1/(B radar bandwidth), we also have

$$\Delta R = \frac{1}{2} c\tau = \frac{c}{2B} \tag{3.5}$$

Obviously, in order to get higher range resolution, the pulse width should be decreased.

3.1.3 Radar Equation

For a radar system, the signal power at the input of the receiver, P_R, is

$$P_R = \frac{P_T G_{DT} G_{DR} \lambda^2 \sigma}{(4\pi)^3 R^4} \tag{3.6}$$

where P_T is transmitted power; R is the signal transmitting distance; λ is the wavelength of the transmitted signal; G_{DT} and G_{DR} are the gain of transmitting and receiving antennas; σ is the effective area of an isotropic target, called radar cross section (RCS).

In practical situations, the received signal is contaminated with noise. The receiver input noise power, N_n, is

$$N_n = kT_s B \tag{3.7}$$

where $k = 1.38 \times 10^{-23}$ *Joule/degree Kelvin* is the Boltzmann's constant; T_s is the total effective receiver noise temperature in degrees Kelvin; B is the receiver bandwidth. So, the signal to noise ratio (SNR) at the input of receiver is

$$SNR_i = \frac{P_R}{N_n} = \frac{P_T G_{DT} G_{DR} \lambda^2 \sigma}{(4\pi)^3 R^4 k T_s B} \tag{3.8}$$

Equation (3.8) is known as the radar equation.

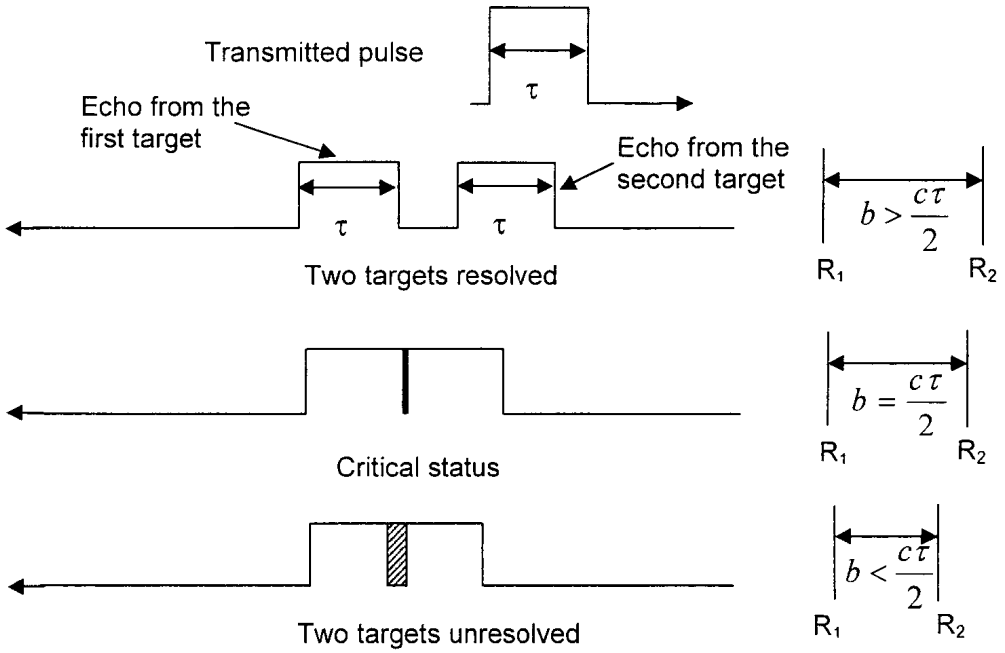

Figure 3.2 Illustration of the range resolution

With a bistatic system, where the transmitter and receiver are placed in separate places, the range, R, in the equation, (3.7) and (3.8) is replaced by $\sqrt{R_t R_r}$ [Meikle,2001]. So we have

$$P_R = \frac{P_T G_{DT} G_{DR} \lambda^2 \sigma}{(4\pi)^3 R_t^2 R_r^2} \tag{3.9}$$

$$SNR_i = \frac{P_R}{N_n} = \frac{P_T G_{DT} G_{DR} \lambda^2 \sigma}{(4\pi)^3 R_t^2 R_r^2 k T_s B} \tag{3.10}$$

where R_t is the distance from the transmitter to the target, and R_r is the distance from the target to receiver.

As we know, for pulsed radar system, the receiver bandwidth is taken to be the reciprocal of the transmitter pulse width, τ. So equation (3.10) can also be written as:

$$SNR_i = \frac{P_R}{N_n} = \frac{P_T \tau G_{DT} G_{DR} \lambda^2 \sigma}{(4\pi)^3 R_t^2 R_r^2 k T_s} \tag{3.11}$$

3.1.4 Pulse Compression

From previous analysis, we know that range resolution can be improved by using short pulses. However, if the peak transmitted power is the same, utilizing short pulses decreases the average transmitted power and then the SNR at the receiver. As it is usually difficult and expensive to increase the peak power, pulse compression techniques are introduced. "Pulse compression allows us to achieve the average transmitted power of a relatively long pulse, while obtaining the range resolution corresponding to a short pulse."[Mahafza, 2005]

Pulse compression can be achieved by frequency modulation or phase modulation. Because of its simplicity of implementation, binary phase coding is widely used. Figure 3.3 shows the diagram of a binary phase coding system. The code sequence is normally with value +1 and -1. After modulation, the transmitted pulse can be seen as a long pulse of width τ', which is divided into N smaller pulses or chips; each is of width $\tau = \tau' / N$. The phase of each chip is either 0 or π. After demodulation, the received echo is correlated with the same sequence. When they match, the correlator produces a maximum output that is N times larger than the peak value of the long pulse. The time of the maximum output determines the range of the target.

If there is no noise and distortion of the signal, the output of the receiver can be seen as the autocorrelation result of the code sequence. Figure 3.4 shows the autocorrelation result of Barker 13 code. Many binary phase codes have been invented. Normally, the codes that yield minimum peak sidelobes in the autocorrelation results are desirable. One criterion is peak sidelobe level (PSL), which evaluates the ratio of the

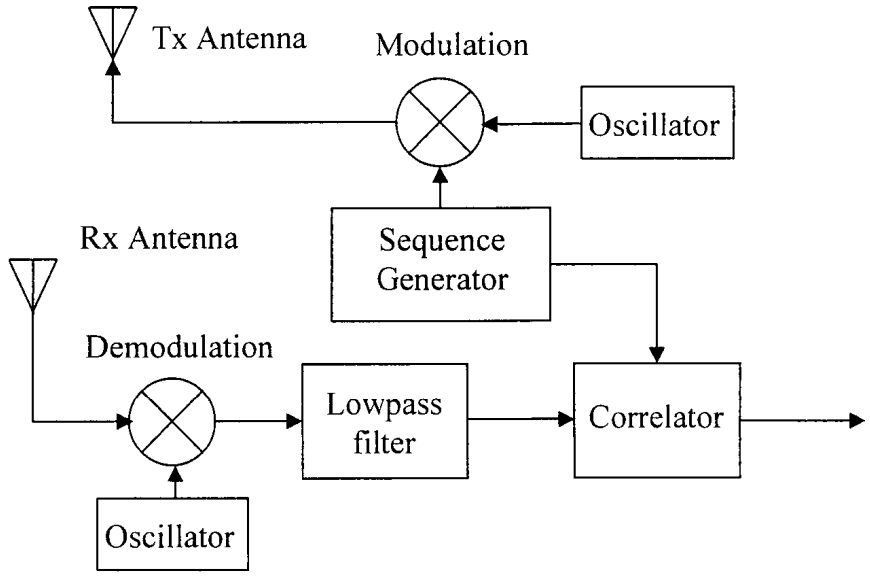

Figure 3.3 Diagram of binary phase coding system

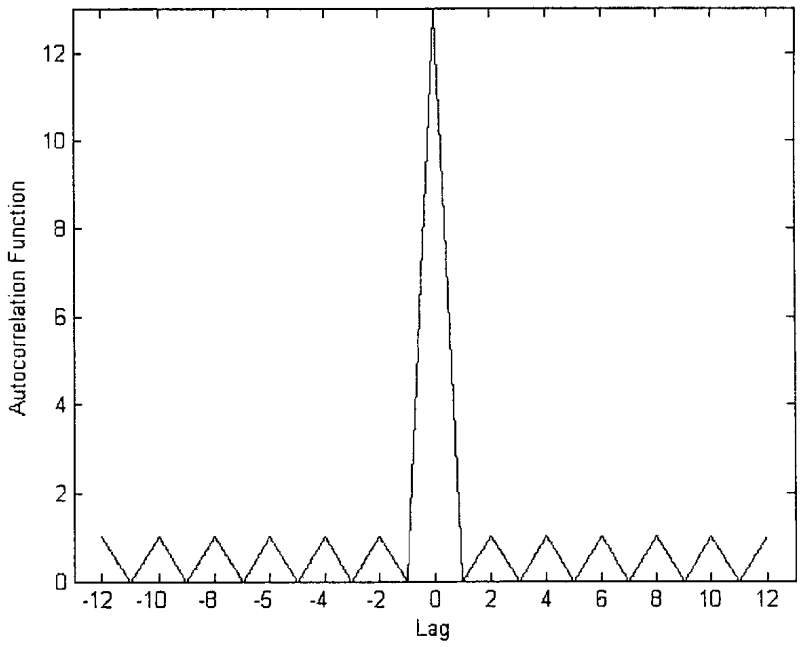

Figure 3.4 Autocorrelation function of Barker 13

maximum sidelobe magnitude to the mainlobe magnitude:

$$PSL = 10\log[\max(\rho_m^2)/\rho_0^2] \tag{3.12}$$

where $\rho_m \quad m \neq 0$ refers to the sidelobe, and ρ_0 is the mainlobe.

Barker 7 and 13 code [Gao, 1991], and Legendre 1019 code have been implemented in CADI [Huang, 2003]. All of them yield the minimum peak sidelobes with the given code length. Their definition is below:

Barker 7: 1 1 1 −1 −1 1 −1

Barker 13: 1 1 1 1 1 −1 −1 1 1 −1 1 −1 1

Legendre: $L(n) = \left(\frac{n}{N}\right) = \begin{cases} +1; & n \text{ is a quadratic residue mod } N \\ -1; & \text{otherwise } (n \text{ is a quadratic non - residue mod } N) \\ 1 \text{ or } -1; & n = 0 \end{cases}$

where N is the desired code length. For code length between 100 and 130, Legendre 101, 103, 107, 109, 113, and 127 are found to be the minimum peak sidelobe codes [Levanon, 2004] [Rao, 1986].

As the phase modulated pulse can be seen as N chips, its range resolution is determined by the width of the chip, τ, and equals to $c\tau/2$ [Mahafza, 2005].

Similarly, the radar equation (3.11) can be written as

$$SNR_i = \frac{P_R}{N_n} = \frac{P_T \tau' G_{DT} G_{DR} \lambda^2 \sigma}{(4\pi)^3 R_t^2 R_r^2 k T_s} = N \frac{P_T \tau G_{DT} G_{DR} \lambda^2 \sigma}{(4\pi)^3 R_t^2 R_r^2 k T_s} \tag{3.13}$$

Obviously the SNR at the receiver side is N times higher than that of the single pulse [Mahafza, 2005]. So, by increasing the total pulse length, pulse compression technique can keep the range resolution unchanged while increasing the SNR by N times. Table 3.1 shows some characteristics of several code sequences.

3.2 The CADI System

The Canadian Advanced Digital Ionosonde (CADI) is an HF pulse radar used to study the properties of ionosphere. CADI was developed more than 10 years ago. After several revisions, it has become a small-size, low-cost and multi-functional digital ionosonde. It is commercially built and has been deployed in several countries. It can extract information from echoes, such as: (1) Amplitude and phase of received signals; (2) Angle of arrival; (3) Range and height of targets; (4) Doppler shift and radial velocity. A network of CADI can provide valuable data for research on F-region, polar cap convection, gravity waves, sporadic-E regions, etc. Table 3.2 shows some of the operating specifications of a CADI system.

3.2.1 Overview of the CADI System

CADI system is mainly composed of a PC, a Direct Digital Synthesizer (DDS) control board, one or several receiver boards, a power amplifier, and antennas. Figure 3.5 shows the block diagram of the CADI system [Jian, 1996] with one receiver. In the figure, 'Tx' refers to the 'Transmitter', and 'RCVR' or 'Rx' refers to the 'Receiver'.

The PC acts as a human interface for the operator to configure the whole system and analyze the data. It also communicates with the microcontrollers to control the system and receive data. The microcontrollers are chosen from 68HC11 family. The one on the DDS board controls the transmitting and receiving sequences, and modulates the signals. The other two on the receiver board sample the received data, correlate the data with the code sequence, and send them to the PC. The DDS chip generates the required carrier frequencies and provides local oscillator signals to the receiver board. In newer versions of CADI, GPS receivers are used to offer external triggering signals and then

synchronize CADI systems.

	Single Pulse	**Barker 13**	**Legendre 113**	**Legendre 1019**
Code length (*N*)	1	13	113	1019
Peak sidelobe level (unit)	N/A	1	7	24
PSL (dB)	N/A	-22.2789	-24.1596	-32.5593
SNR improvement (dB)	0	11.1	20.5	30.1

Table 3.1 Characteristics of several codes

Frequency Range	1~20MHz
Transmitting Power	Max. 600W
Pulse Width	40μs
Pulse Repetition Frequency	20 or 40Hz
External GPS trigger	Available
Range Resolution	6Km
Maximum Measurement Range	1020Km
Pulse Compression	Complementary, Barker code
Number of Receivers	Up to 4

Table 3.2 Specifications of CADI system

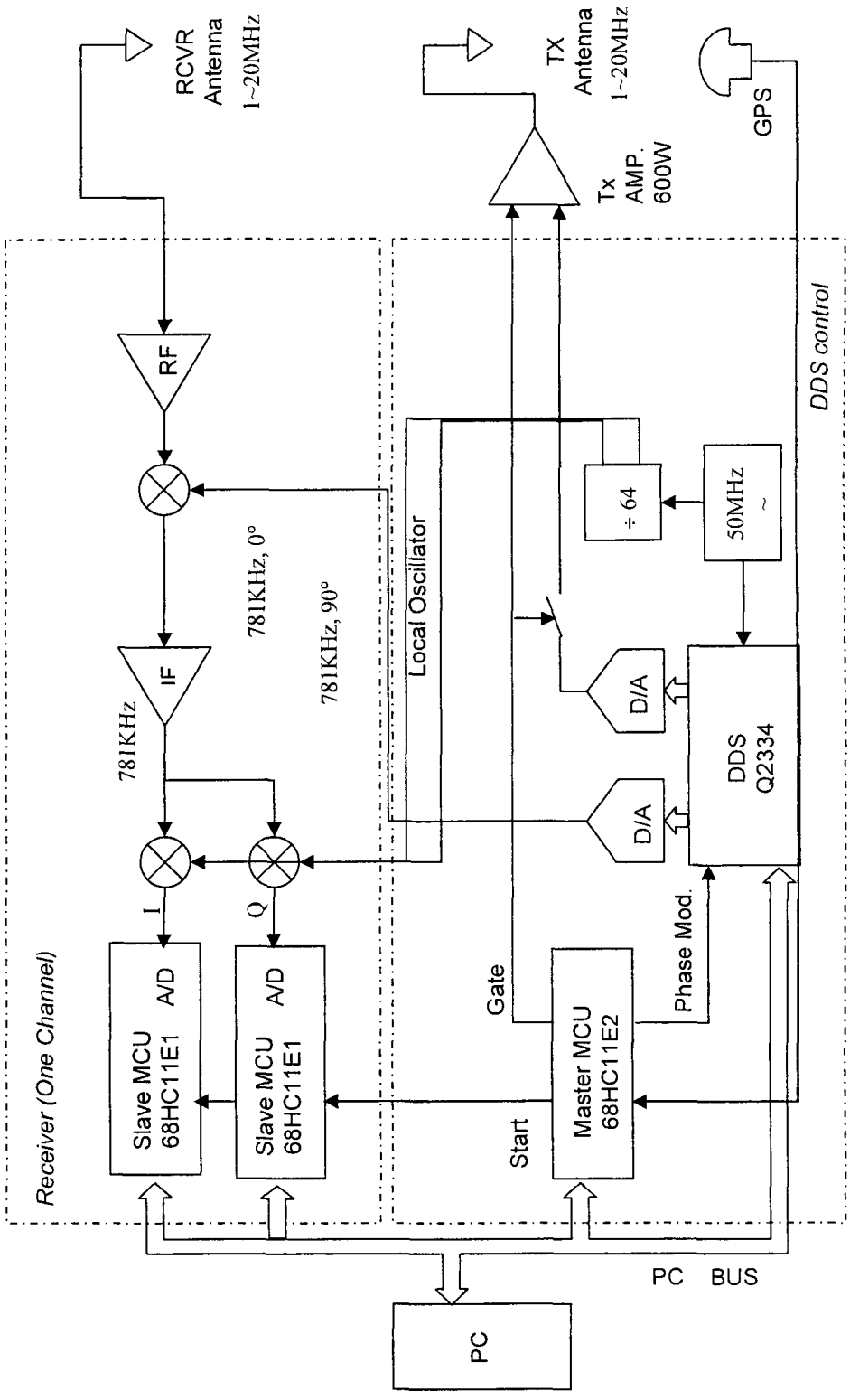

Figure 3.5 Diagram of CADI

3.2.2 Operation Modes

CADI can work in several different modes. The 3 basic operation modes are ionogram mode, height versus time mode and Doppler sample mode. In ionogram mode, the frequency of the transmitted signals starts from 1 MHz and is increased up to 20 MHz. The result produces height versus frequency plots, called ionograms. In height versus time mode, the radar works at a fixed frequency and generates a height versus time plot. Doppler sample mode is chosen if motion analysis is required. The system works at a fixed frequency. The echo is collected at a specific sampling frequency and then Doppler information is extracted. In this project, CADI will work as a receiver for oblique sounding and generate height versus time plot. Details will be given in Chapter 5.

3.2.3 Signal Processing in the Receiving Board

Since CADI works as a receiver in this project, it is desirable to know the signal processing in the receiving board. As in Figure 3.5, after mixed with the local oscillator, the signal can be written as:

$$R(t) = V_r \cos[2\pi f_o t + \phi(t)] \tag{3.14}$$

where: V_r is the amplitude, f_o is the intermediate frequency (IF), and $\phi(t)$ is the phase.

Reference signals to I channel and Q channel are:

$$I_0(t) = \cos 2\pi f_o t \tag{3.15}$$

$$Q_0(t) = \sin(-2\pi f_o t) \tag{3.16}$$

The received signal is split into two parts and mixed with I and Q reference signals:

$$RI(t) = R(t) \times I_o(t) = \frac{1}{2} V_r [\cos(4\pi f_o t + \phi(t)) + \cos(\phi(t))] \tag{3.17}$$

$$RQ(t) = R(t) \times Q_o(t) = \frac{1}{2} V_r[-\sin(4\pi f_o t + \phi(t)) + \sin(\phi(t))] \quad \textbf{(3.18)}$$

For simplicity, replace $\frac{1}{2} V_r$ with V_r. After low-pass filtering, the first terms are removed. Then through A/D Sampling, the signal is digitized and can be written as:

$$I_n = V_r \cos(\phi(t_n)) \quad \textbf{(3.19)}$$

$$Q_n = V_r \sin(\phi(t_n)) \quad \textbf{(3.20)}$$

Then the magnitude and phase of the signal can be obtained:

$$C_n^2 = I_n^2 + Q_n^2 \quad \textbf{(3.21)}$$

$$\varphi_n = \arctan \frac{Q_n}{I_n} \quad \textbf{(3.22)}$$

A/D sampling starts at the same time that CADI starts transmitting. The sample rate is each 20us. The maximum number of samples for each sounding is 340 for I and Q channel respectively, which means the maximum detectable range is $\frac{340 \times 20 \times 10^{-6} \times 3 \times 10^5}{2} = 1020km$. The sampled data is saved in the two slave microcontrollers. The microcontrollers can be configured to correlate the data with the code sequence and send the results back to PC, or send the raw data to PC.

Chapter 4. Design of the New Transmitter

This chapter gives detailed description of the transmitter, including the hardware and software design.

4.1 Requirements

This transmitter is designed and developed for the e-POP Tomography mission. It will transmit signals to the e-POP satellite. The data collected by RRI will be used to demonstrate the HF Tomography.

In Wang's theory [Wang, 2006], the initial phase problem inherent in other current ionospheric tomography methods and the ambiguity problem can be eliminated by measuring differential Faraday rotations between two signals from a same transmitter. In order to restrict the differential Faraday rotations in the range of 2π, the frequencies of these two signals should be close to each other. Based on her simulations, the proposed frequencies are 18MHz and 17.985MHz, and should be able to be changed by users. As for the transmitting power, the minimum SNR of the signals detectable by the probes of RRI should be higher than 20dB, and the input dynamic range of RRI receivers is from -100 to 0dBV. According to Wang's calculation, with a transmitting power of 7W, the signal level at the input of the RRI will be -46dBV, and the SNR is 46dB. Therefore it can satisfy this requirement. HF Tomography algorithm needs signals from several transmitters displaced in different places. In order to be distinguishable from other transmitters, each transmitter should transmit in a fixed time slot and be synchronized with the others [Wang, 2006]. Figure 4.1 illustrates the time schedule of a 5-transmitter ionospheric tomography system for the e-POP mission. The start point is the GPS PPS

signal. Each transmitter transmits a 10ms long pulse every 125ms. The time interval between transmitters is 25ms.

As this transmitter will be tested with CADI, its performance should also be comparable with that of CADI. The frequency range should go from 1 to 20MHz. The SNR of the signals at the receiver side should at least be in the same level with normal CADI signals so that the signals can be detected by a CADI receiver.

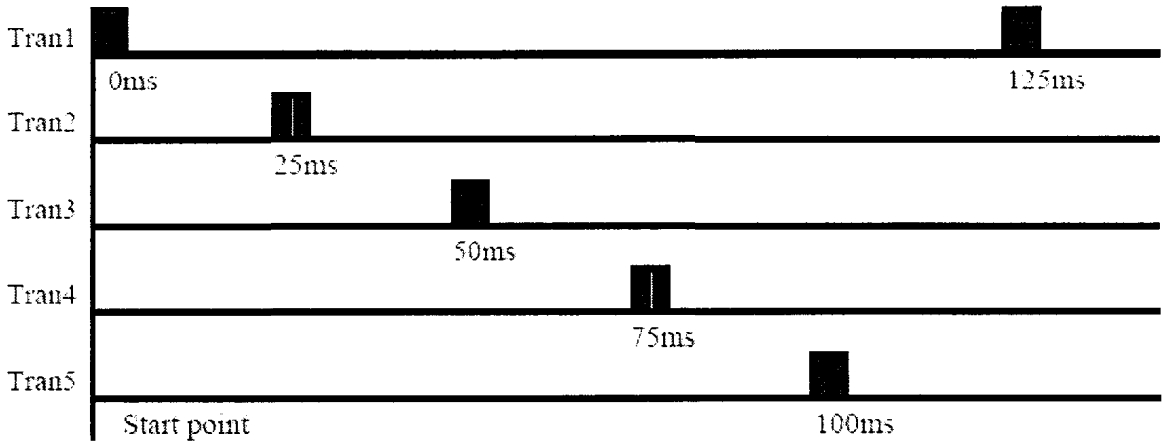

Figure 4.1 Time schedule for a 5-transmitter ionospheric tomography system

4.2 Overview of the Transmitter

The block diagram of the transmitter is shown in Figure 4.2.

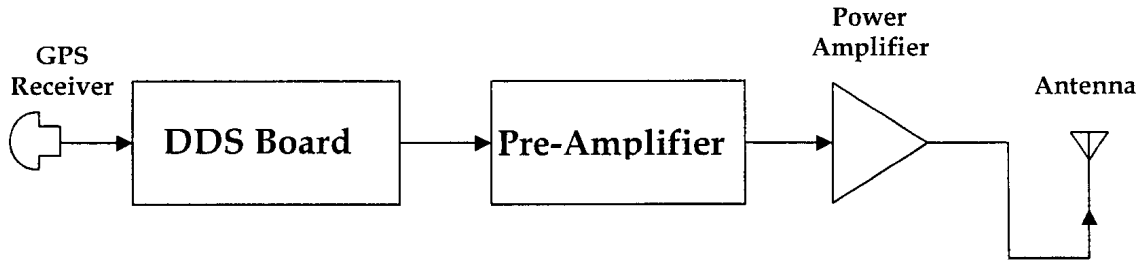

Figure 4.2 Diagram of transmitter

A GPS receiver can generate a Pulse Per Second (PPS), which is utilized to synchronize the transmitters. The microcontroller on the DDS board can accept the configuration from users and control the transmitter. The DDS board can generate two

signals, which can be set between 1MHz and 20MHz. At 4MHz, the pre-amplifier amplifies the signal to about 600mW. After the power amplifier, the power of the signal will be up to around 34W. At 18MHz, the transmitted power is 15W. According to equation (3.13),

$$SNR_i = \frac{P_R}{N_n} = \frac{P_T \tau' G_{DT} G_{DR} \lambda^2 \sigma}{(4\pi)^3 R_t^2 R_r^2 k T_s} = N \frac{P_T \tau G_{DT} G_{DR} \lambda^2 \sigma}{(4\pi)^3 R_t^2 R_r^2 k T_s} \quad \textbf{(4.1)}$$

if all other factors do not change, the SNR at the receiver side depends on the product of the number of chips, N, and the peak transmitting power, P_T. In previous studies, it was demonstrated that, at 4MHz, CADI system could work at as low as 1W with Legendre 1019 code [Huang, 2003]. The product of NP_T was therefore 1019. This transmitter can be configured to transmit a Legendre 113 sequence. At 4MHz, the product is $34 \times 113 = 3842$, which means the SNR at the receiver side will be around 4 times as large as for the 1W signal that could be detected by CADI.

After power is on, the microcontroller on DDS board reads in the configuration set up by the users and initializes the two DDS chips. When GPS PPS signal arrives, the microcontroller waits until the desired transmitting time slot, then turns on the RF switches, and starts transmitting.

4.3 GPS

A GPS receiver is connected to the microcontroller on the DDS board. The receiver provides a Pulse per Second (PPS) signal, which triggers the microcontroller once per second. This triggering signal provides the same start point to all the transmitters and then synchronizes them. GARMIN 35 LVC and GARMIN 18 LVC GPS receivers are used in the project.

4.4 DDS Board

As shown in Figure 4.3, DDS board mainly consists of input panels (configuration dip switches), a microcontroller, two DDS chips, two low-pass filters, two RF switches, a power combiner, and an amplifier. The microcontroller reads users' input from the panel and controls the transmitting process. DDS chips, low-pass filters and switches generate the desired pulsed signal. DDS chip 1 generates the lower frequency, while chip 2 generates the higher one. Then the two signals are combined together and amplified before they are fed to the pre-amplifier. Figure 4.4 shows the schematic of the DDS board.

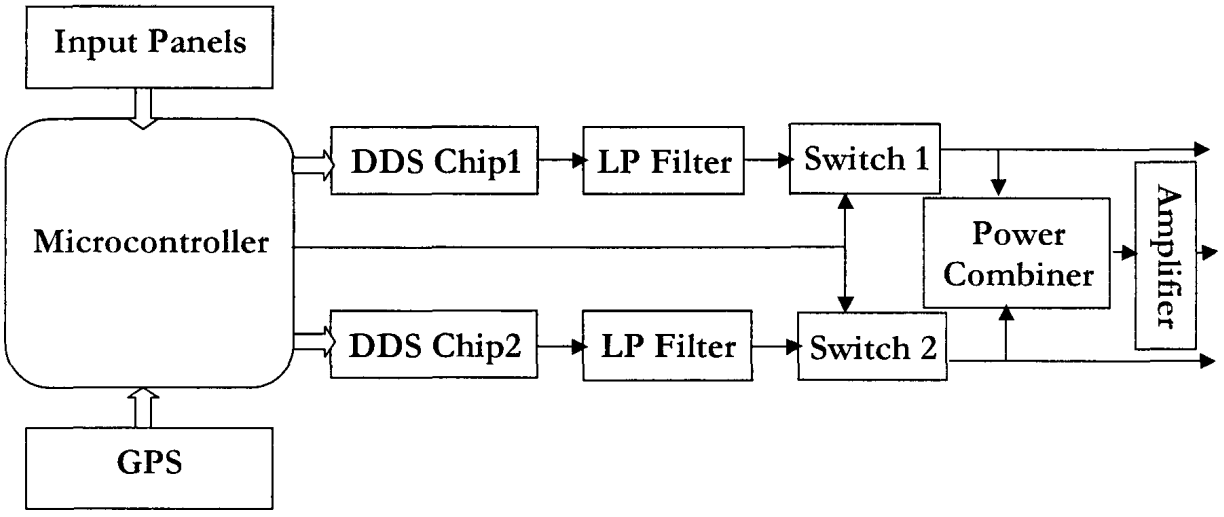

Figure 4.3 Block diagram of DDS board

4.4.1 Input Panel

There are three DIP switches panels on a board. With them, users can set up the working parameters:

1) Higher frequency of the dual-frequencies: 0.1MHz to 20.0MHz

2) Frequency difference between the dual frequencies: maximum 7 values can be set up.

3) Transmitter number: 0-7.

4) Desired transmitting code: maximum 4 different codes can be chosen. Single,

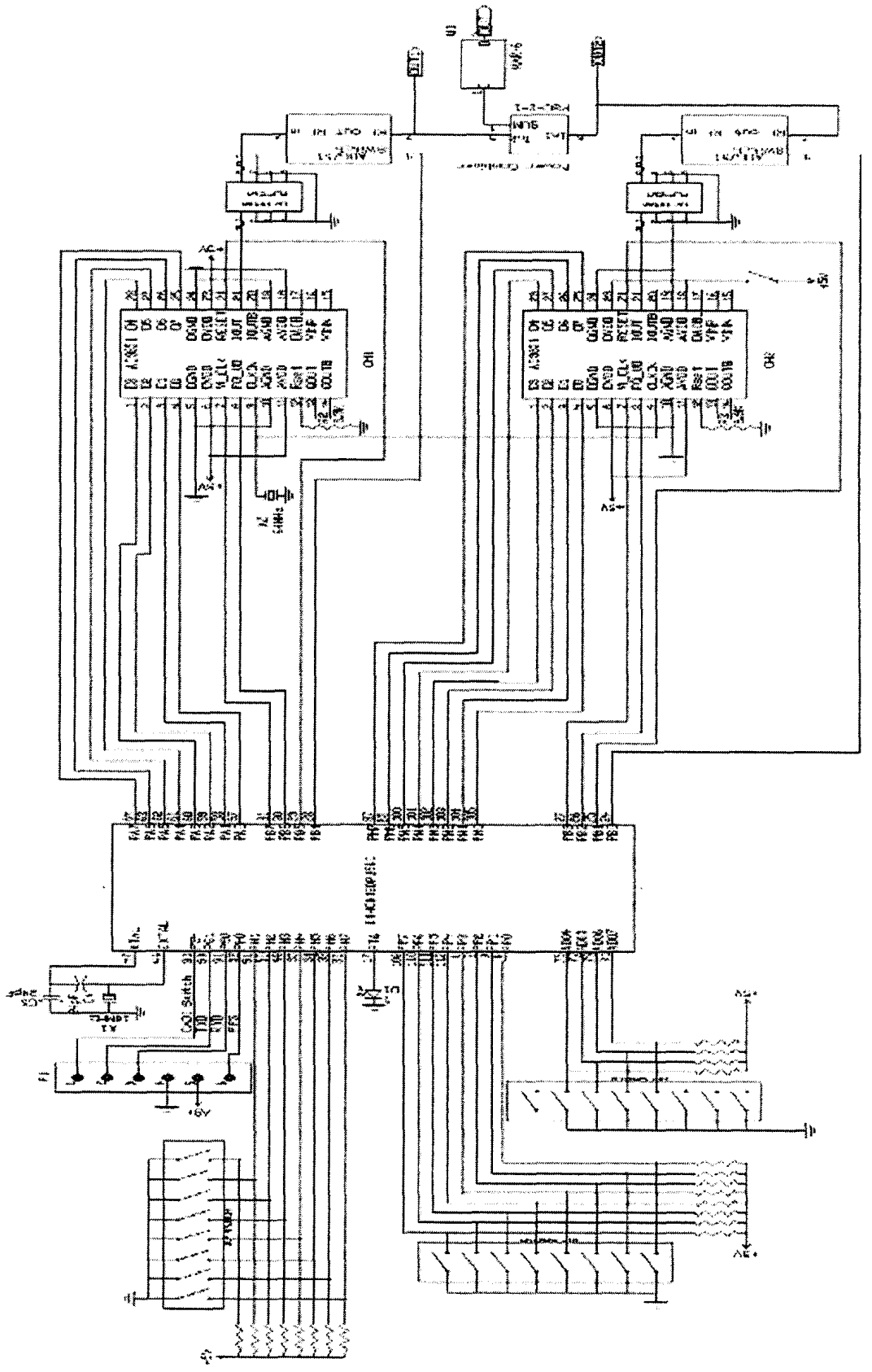

Figure 4.4 Schematic of the DDS Board

Barker13, Legendre 113, and Legendre 127 are now available.

4.4.2 Microcontroller

A. Hardware Description

A module, Adapt9S12DP256, developed by Technological Arts is plugged on to the DDS board. This module is a modular implementation of Freescale Semiconductor's MC9S12DP256C microcontroller chip. Two 50-pin connectors bring out all the I/O lines from MCU and make it very easy to connect the module to other boards. The external clock is provided by a 16MHz crystal on board. A universal 6-pin Background Debug Mode (BDM) connector support BDM pods from multiple vendors.

The MC9S12DP256C microcontroller unit (MCU) is a 16-bit device composed of standard on-chip peripherals including a central processing unit, 256K bytes of Flash EEPROM, 12K bytes of RAM, 4K bytes of EEPROM, and 89 discrete digital I/O channels. The MCU can operate in several modes. In this project, it works in single-chip mode. In this mode, the MCU functions as a self-contained microcontroller and has no external address or data bus so that the circuit is very simple.

The microcontroller incorporates twelve ports which are used to control and access various devices subsystems. When not used for these purposes, the ports can be configured as general-purpose I/O interfaces. In this design, Port A, B, M, T, S, H, P, and AD0 are used. Table 4.1 shows the configuration and usage of these ports. PT6 is connected to a LED, which is turned on when the transmitter starts transmitting and turned off when the transmitting is over. PH0 is configured as an IRQ pin. When the rising edge of GPS PPS signal is detected, the MCU goes into the interrupt service routine (ISR). Port S [1:0] and PortAD04 are reserved for future uses.

B. Software Description

The flowcharts of the MCU programs are shown in Figure 4.5 and Figure 4.6. In

Port Name	Data Direction	Description
Port A[7:0]	Out	Send out tuning words to the DDS chip 1
Port M[7:0]	Out	Send out tuning words to the DDS chip 2
Port B[7:5]	Out	Provide W_CLK, FQ_UD, and Reset signals to DDS chip1
Port B[4]	Out	Provide Turn on/off signal to Switch 1
Port B[3:1]	Out	Provide W_CLK, FQ_UD, and Reset signals to DDS chip2
Port B[0]	Out	Provide Turn on/off signal to Switch 2
Port T[6]	Out	Turn on/off LED when switches are on/off
Port S[4]	Out	Turn on/off the switch of CADI power amplifier
Port S[1:0]	Out	Reserved for communication with GPS receiver
Port H[7:4]	In	Read in the decimal part of the higher one of the dual frequencies
Port H[3:1]	In	Read in the frequency difference of the dual frequencies
Port H[0]	In	Receive GPS PPS signal
Port P[6:2]	In	Read in the integral part of the higher one of the dual frequencies
Port P[1:0]	In	Read in the code type users choose
Port AD0[7:5]	In	Read in the transmitter number
Port AD0[4]	In	Reserved for future use

Table 4.1 Configuration of 9S12 microcontroller ports

the main program, after power is on, the MCU reads in the configuration, calculates the lower frequency and the start time of the transmission, and sets up the code pattern. Next, MCU initializes the DDS chips and then waits for the PPS signal. When the PPS signal

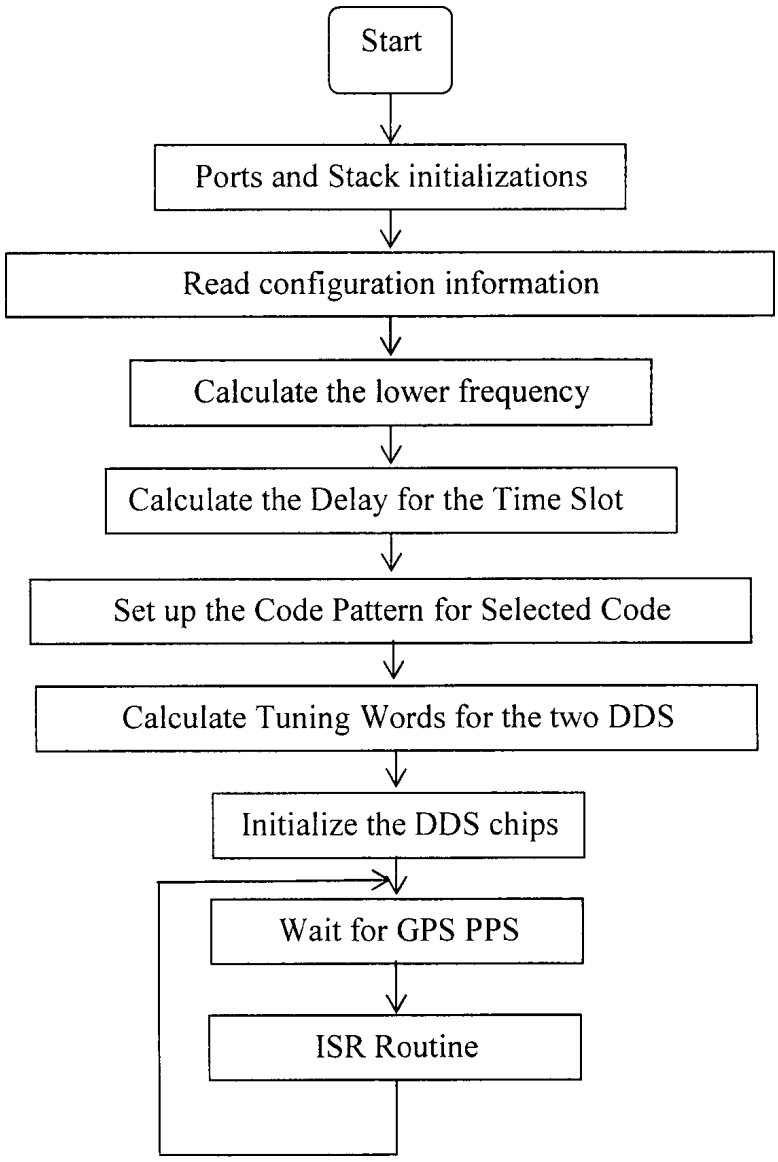

Figure 4.5 Flowchart of microcontroller main program

arrives, MCU goes into the ISR. In the ISR, first, it waits until the allocated time slot. Then, it sends out the tuning words and control signals to DDS chips for the first code. Next, it turns on the switches and LED. After the whole code sequence is transmitted, switches and LED are turned off. MCU returns to wait for another PPS signal.

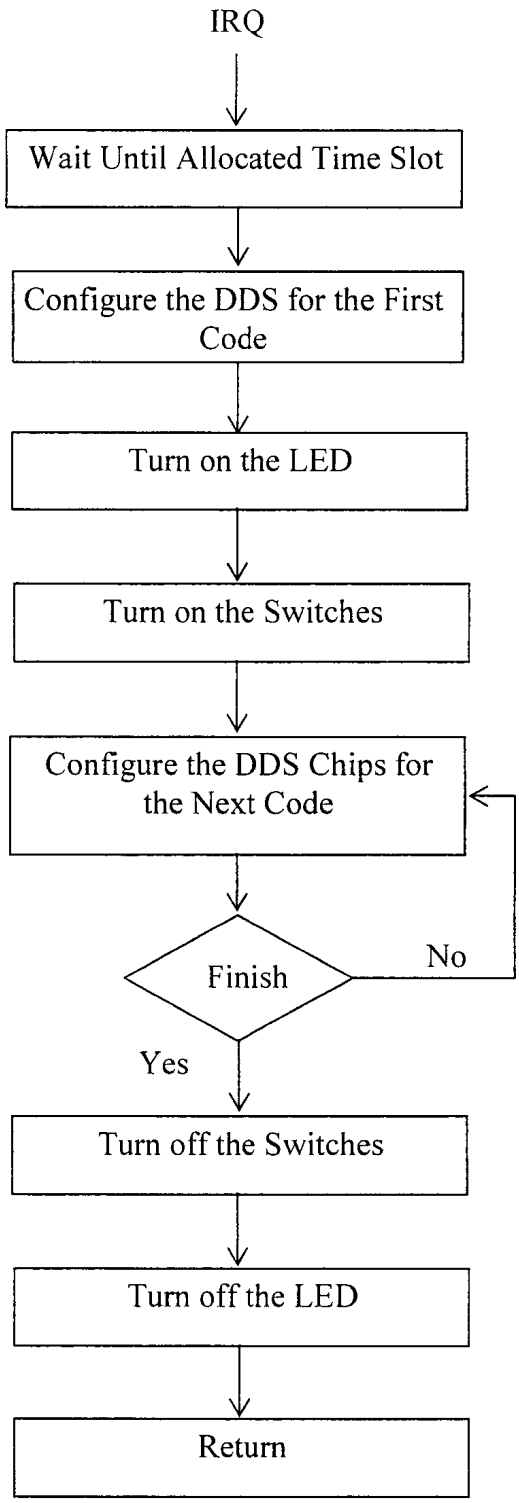

Figure 4.6 Flowchart of the microcontroller ISR routine

4.4.3 DDS Chip

A. Principle of DDS

DDS has better performance than traditional frequency synthesis methods. With the improvement of the theory and IC circuit technology, it becomes more and more popular. The way most of the DDS chips work is: first, the chip accepts an input value; next, a phase accumulator increments the phase value, which is determined by the input value, in each work clock; then, in each clock, sine wave amplitudes are read out according to the phase value; finally, this digitalized sine wave is transformed to an analog wave. The basic idea is the final output frequency is determined by the input value.

Suppose a pure sine wave is:

$$u(t) = \sin(2\pi f_0 t) = \sin \omega_0 t = \sin \theta(t) \tag{4.2}$$

Its phase is a linear function of time:

$$\theta(t) = \omega_0 t = 2\pi f_0 t \tag{4.3}$$

The derivative of the phase is a constant, i.e. the frequency:

$$\frac{d\theta(t)}{dt} = \omega_0 = 2\pi f_0 \tag{4.4}$$

The amplitude and phase of the sine wave are shown as solid line in Figure 4.7. If it is sampled with frequency $f_s = 1/T_s$, the result is

$$u^*(m) = \sin(2\pi f_0 m T_s), \qquad m = 0,1,2,\cdots \tag{4.5}$$

The phase function therefore becomes

$$\theta^*(m) = 2\pi f_0 m T_s = \Delta\theta \cdot m \tag{4.6}$$

where $\Delta\theta = 2\pi f_0 T_s = 2\pi \frac{f_0}{f_s}$ is the phase increase between two samples. The slope of the phase increase is $\frac{\Delta\theta}{\Delta t} = \frac{\Delta\theta}{T_s} = 2\pi f_0$. According to the sampling theory, as long as $f_0/f_s < 1/2$, the continuous wave can be reconstructed from the sampled values which are shown as black dots in Figure 4.7. If the sampled values stay constant during the sampling interval, the sampled wave is shown as the segment-line in the figure.

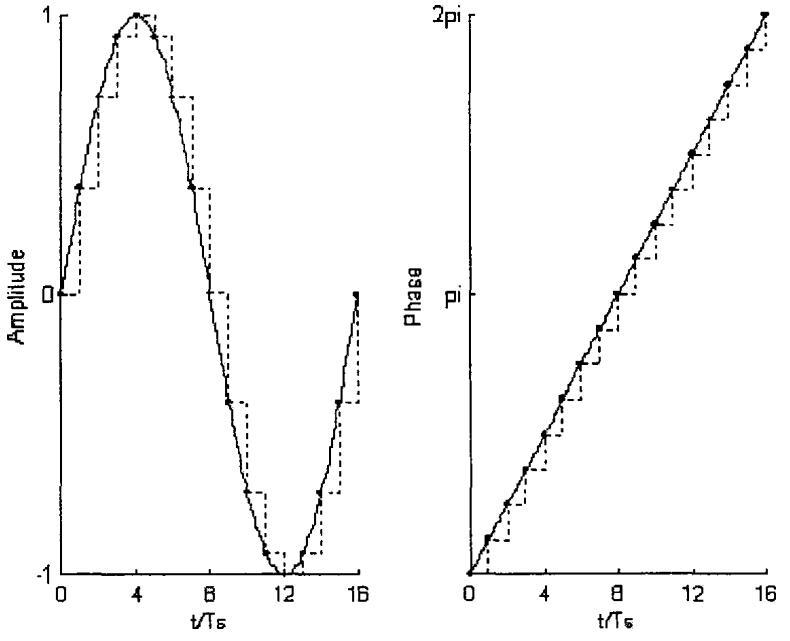

Figure 4.7 Sampled amplitude and phase of a sine wave

From above, it is obvious that the frequency of the signal has a linear relation with the slope of the phase increase; when sampling frequency is fixed, the slope is determined by the phase increase $\Delta\theta$. So, the frequency can be controlled by the phase increase. Suppose 2π is divided by an arbitrary large constant integer value M, we get $\delta = 2\pi/M$, which is the minimum phase increase. Then we can obtain:

$$\sin(2\pi f_0 m T_s) = \mathrm{Im}\left[\exp\left(j\frac{2\pi}{M}m\right)\right], \quad m = 0,1,2,\cdots,M-1 \qquad \textbf{(4.7)}$$

So the lowest output frequency is

$$f_{0\min} = \frac{1}{MT_s} = \frac{f_s}{M} \tag{4.8}$$

If the phase increase is $k\delta$, the output frequency becomes

$$f_0 = kf_s / M \tag{4.9}$$

After filtering, the analog signal is $u(t) = \sin(2\pi \frac{k}{M} f_s t)$. k is called the frequency control word. When the sampling frequency, f_s, and M are fixed value, the frequency of the analog signal is determined by k.

B. AD9851

AD9851 is designed based on the theory above. Its block diagram is shown in Figure 4.8 [Analog Device Inc., 2004]. The incremental frequency resolution is determined by the frequency of the reference clock (the sampling frequency, f_s) divided by $M = 2^{32}$. The phase accumulator is a variable-modulus counter. It reads in the frequency tuning word, k, which has N=32 bits, and increments the number stored in the counter by the value of the tuning word each time it receives a clock pulse. When the counter overflows, it wraps around, making the phase accumulator's output contiguous. Then, the AD9851 uses an algorithm that converts the output of the phase accumulator to an appropriate COS amplitude value. Next, the digitalized output of the DDS block drives the internal high speed D/A converter that reconstructs the wave in analog form. After filtering, the pure sine wave at the specified frequency can be obtained.

As the frequency control word has N bits, and its value is k, the output of the phase accumulator at $t = nT_s$ is

$$\theta(n) = nk \bmod 2^N, \qquad n = 0,1,2,\cdots \tag{4.10}$$

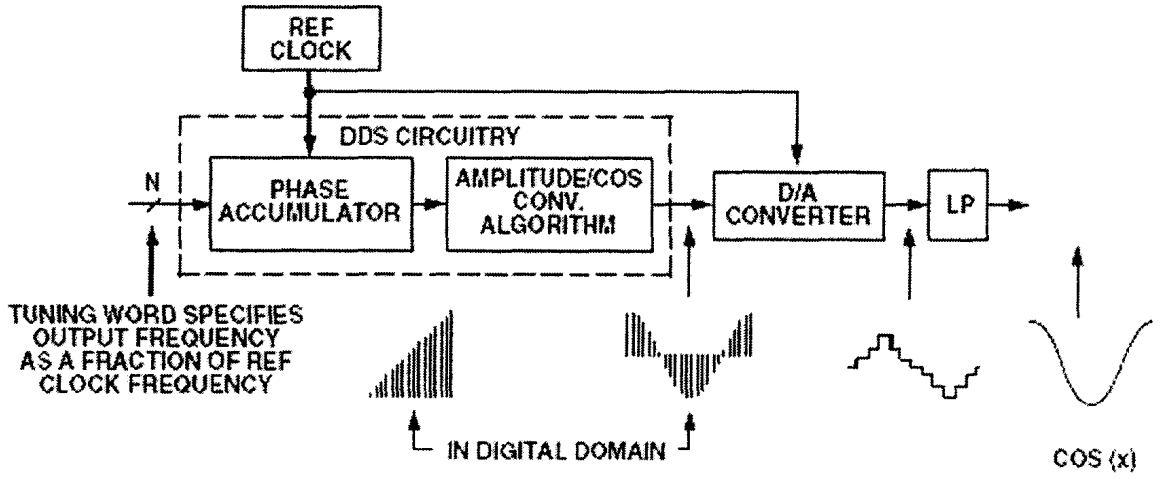

Figure 4.8 Block diagram of AD9851

Its period is $\mu = \dfrac{2^N}{Gcd(2^N,k)}$, where $Gcd(2^N,k)$ means the greatest common divisor of 2^N and k. The output of the DDS circuitry can be written as

$$s(n) = \cos(\frac{2\pi}{2^N} \cdot kn), \ n = 0,1,2,\cdots \tag{4.11}$$

Its period is also μ. After DAC, the analog signal $s(t)$ is obtained, whose period is μT_s. Within the period $[0, \mu T_s]$, it can be expressed as:

$$s(t) = \sum_{n=0}^{\mu-1} \cos(\frac{2\pi}{2^N} \cdot kn) q(nT_s), \qquad 0 \le t \le \mu T_s \tag{4.12}$$

where $q(nT_s)$ is a rectangular function: $q(nT_s) = U(t - nT_s) - U(t - (n+1)T_s)$. The Fourier transform of $s(t)$ is

$$\begin{aligned} S(\omega) = {} & \pi \sum_{l=-\infty}^{\infty} Sinc(\frac{lf_s - f_0}{f_s}\pi) \cdot \exp(-j\frac{lf_s - f_0}{f_s}\pi) \cdot \delta(\omega + 2\pi f_0 - 2\pi l f_s) \\ & + \pi \sum_{l=-\infty}^{\infty} Sinc(\frac{lf_s + f_0}{f_s}\pi) \cdot \exp(-j\frac{lf_s + f_0}{f_s}\pi) \cdot \delta(\omega - 2\pi f_0 - 2\pi l f_s) \end{aligned} \tag{4.13}$$

where $f_0 = \frac{k}{2^N} f_s$, $Sinc(x) = \frac{\sin x}{x}$. From equation (4.13), it is obvious that the output spectrum contains the fundamental plus aliased signals that occur at multiples of the reference clock frequency (sampling frequency) $\pm$ the selected output frequency, and has a sinc function shape. The spectrum for a reference clock at 100MHz and the output frequency at 20MHz is shown in Figure 4.9 [Analog Device Inc., 2004].

As can be seen, the aliased images are very prominent. So a low-pass filter is generally placed after the output of D/A converter to get the pure sine wave. In order to avoid including aliased signals in the output and ease the complexity of the external filter requirement, the selected output frequency is limited to below 33% of the reference clock frequency in the AD9851. As the maximum frequency of the transmitter should be at least 20MHz, a 64MHz oscillator is utilized in the design.

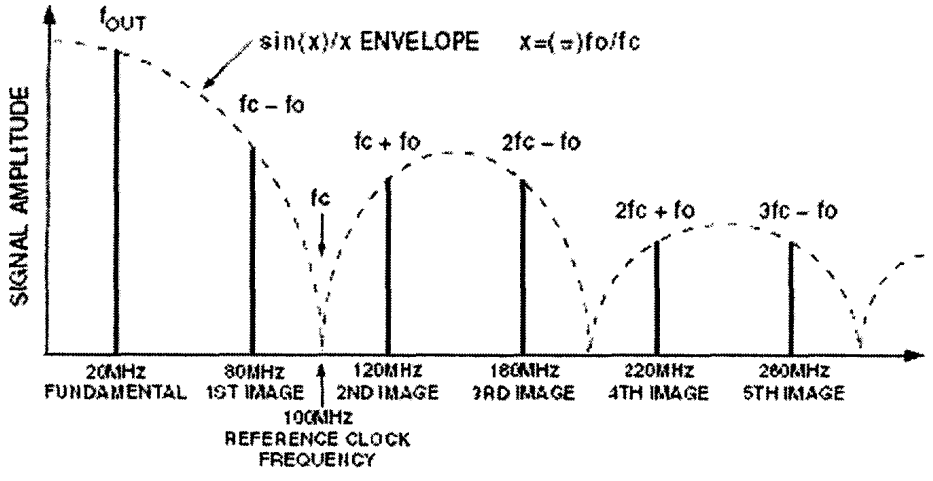

Figure 4.9 AD9851 output spectrum of a sample wave at 20MHz

C. Control AD9851

As required by the AD9851, the microcontroller calculates the tuning words by the formula:

$$Tuningword = \frac{f_{out}}{CLKIN} \times 2^{32} \quad \textbf{(4.14)}$$

where CLKIN is the input reference clock frequency in MHz, in this case: 64MHz. f_{out} is the output frequency in MHz. Tuning word is 32 bits long.

AD9851 contains a 40-bit register that is used to program the 32-bit frequency control word, the 5-bit phase modulation word and the power-down function. The parallel load mode is implemented and five iterations of loading 8-bit word are required. The time sequence is shown in Figure 4.10 [Analog Device Inc., 2004]. When W_CLK rising edges are captured, 8-bit data are loaded and the pointer is moved to the next input register. After five loads, W_CLK edges are ignored until either a reset or an FQ_UD rising edge arrives. The rising edge of FQ_UD loads the 40-bit control data word into the device and resets the address pointer. After it reads the control word, AD9851 generates the signal at the specified frequency.

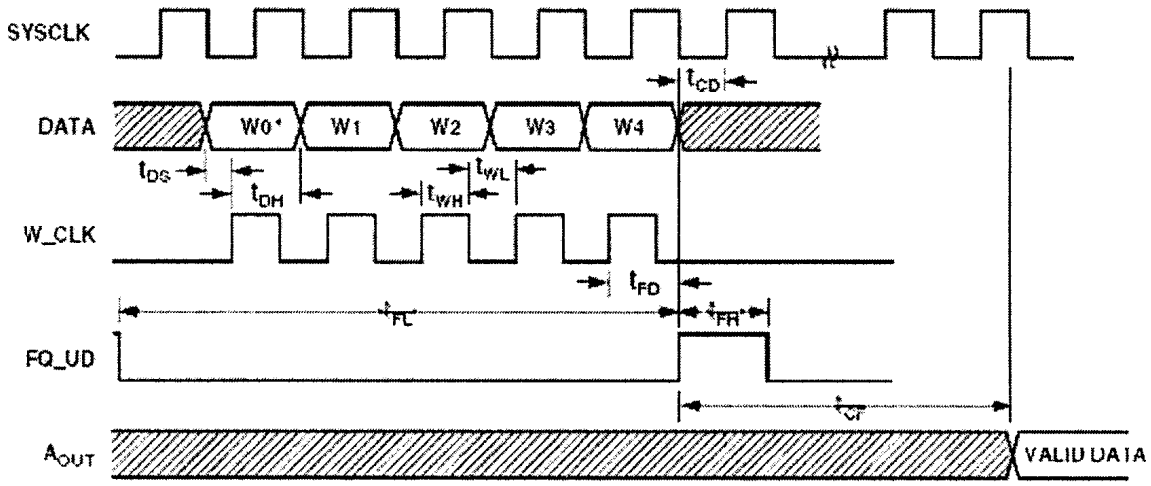

Figure 4.10 AD9851 parallel frequency upload timing sequence

4.4.4 Low Pass Filter

As stated in the previous section, the spectrum of AD9851 contains the fundamental plus aliased signals that occur at multiples of the reference clock frequency

(sampling frequency) ± the selected output frequency. Therefore, a low pass filter is required to work with the DDS9851 chip in order to obtain the desired pure sine wave. Because the frequency of the reference clock is 64MHz, and the frequency range of the desired signals is from 1 to 20MHz, the lowest frequency of the aliased signals is 44MHz.

The low pass filter, PLP21.4 from Mini-circuit, is implemented in this design. Its pass band is DC to 22MHz. The stop band is from 32MHz to 200MHz. The loss is less than 1dB in the pass band while the attenuation is more than 40dB from 41MHz to 200MHz.

4.4.5 RF Switch

An RF switch is placed after the low pass filter to convert the continuous signal to a pulsed signal. ADG751BRM from Analog Device is chosen. The ADG751 is a low voltage single-input-single-output switch. It is constructed in a T-switch configuration, which results in excellent Off Isolation while maintaining good frequency response in the ON condition. Figure 4.11 shows the performance of this chip. In the ON status, the -3dB bandwidth is 180MHz; the maximum ON resistance is 40 Ω . In the OFF status, the isolation between the input and output is lower than -100dB under 20MHz. Status of the switch is controlled by a digital input. When the digital input is high, the switch is off, and vice versa. It works fine with a CMOS level control signal. Therefore this digital control input is provided by the microcontroller directly. This switch works very fast. Its switching time of ON and OFF is 9ns and 3ns respectively. When working with e-POP, the pulse width is 10ms; when testing with CADI, the transmitter can transmit various length pulses, and the single chip width is 40us. Obviously, the switching time is very small compared to the pulse width and can be ignored.

4.4.6 Power Combiner

PSC-2-1 of Mini-circuit is used as a power combiner to combine the two signals. Its frequency range is from 0.1MHz to 400MHz. The phase unbalance and amplitude unbalance between two channels is 3 degree and 0.2dB in the range of 1 to 200MHz. When the two DDS chips produce two 4MHz sine waves with the same initial phase, the output of PSC-2-1 is still at 4MHz and has the same phase with the input. The amplitude of the output is almost the same as the sum of the outputs when these two inputs are fed in independently. When two 4MHz sine waves with inverse initial phase are fed in, there is no output. Figure 4.12 is the result from HP Spectrum Analyzer 8590A. It shows the frequency spectrum of the output of the power combiner with two sine wave inputs- 17.985 MHz and 18MHz. The frequency scale is 15 KHz per division. This figure shows that there are no other frequency components in the output and the strengths of the two signals are almost the same. These experiment results demonstrate that the power combiner works perfectly.

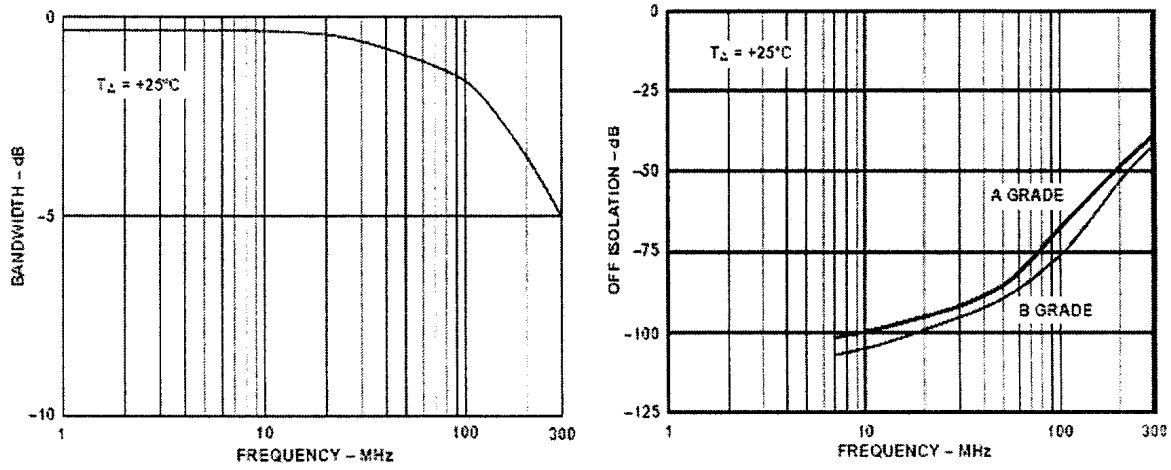

(a) On Response vs. Frequency (b) Off Isolation vs. Frequency

Figure 4.11 Performance of ADG751BRM

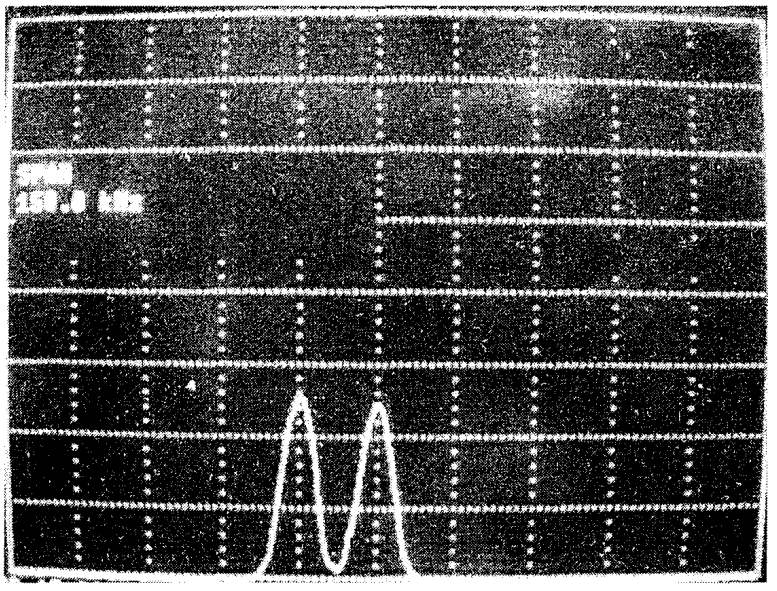

Figure 4.12 Spectrum of the output of PSC-2-1 with two inputs:18MHz and 17.985MHz

4.4.7 Small Signal Amplifier

The power of the output signal of the PSC-2-1 is around -20dBm or 0.01mW, which is too low for the pre-amplifier. So, a small signal amplifier, MAR6+ from Mini-circuit, is placed after the power combiner. The MAR6+ is a monolithic wideband amplifier. It can work in the range of DC to 2GHz. With -20dBm input, the power of the output signal is around 5dBm (3.2mW) at 4MHz and 3dBm (2.0mW) at 20MHz. Because the pre-amplifier is saturated with input at this power level, the signal goes through a 6dB pi attenuation network before it is fed to the pre-amplifier. Therefore the power of input signal to the pre-amplifier is around -1dBm (0.8mW) at 4MHz and -3dBm (0.5mW) at 20MHz.

4.5 Pre-Amplifier

The pre-amplifier is the ZHL-32A from Mini-circuit. Its frequency range is 0.05 to 130MHz; the minimum power gain is 25dB. It is placed after the DDS board and

amplifies the signal to around 28dBm (640mW) at 4MHz and 25dBm (320mW) at 20MHz.

4.6 Power Amplifier

The power amplifier is designed by Mike Kossor. It covers 1.8 to 39MHz. With 28VDC and 1W input, its output can go up to 40W. Figure 4.13 shows the schematic of the power amplifier. It consists of two power MOSFETs chips, IRF510, and is biased for class AB linear operation [Kossor, 2001].

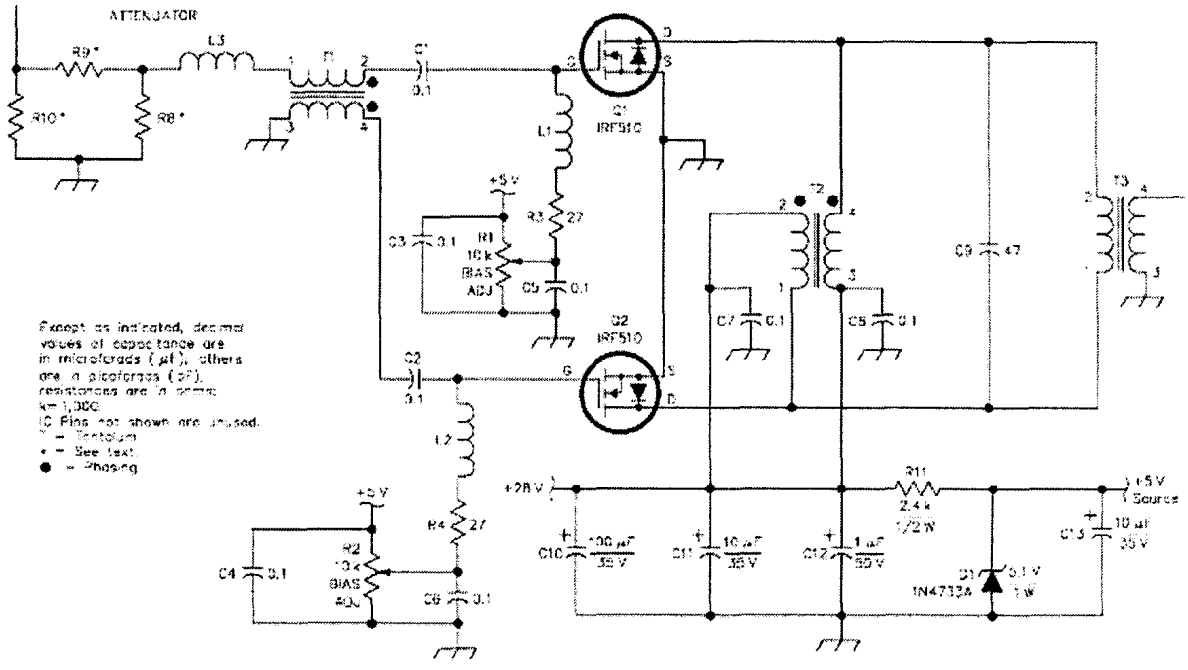

Figure 4.13 Schematic of the power amplifier [Kossor, 2001]

This amplifier exhibits some degree of non-linearity. The two MOSFETs chips work in push-pull. This design cancels the even-order harmonics but not the odd-order harmonics. This results in wave distortion at some frequencies. To resolve this problem, a low-pass filter is needed.

A 5-element Chebyshev low-pass filter is chosen for this design, because it is easy to construct and will satisfy the requirements where the amplitude response is of primary interest. The schematic diagram of the filter is shown in Figure 4.14. As this amplifier's working frequency is around 18MHz, a design with cutoff frequency at 22MHz is chosen [Wolfgang, 2001]. The value for the capacitors and inductors are: *C1=C5=150pF, C3=270pF, L2=L4=498nH.* In the real circuit, a 470nH inductor is used, because it is the closest standard value available.

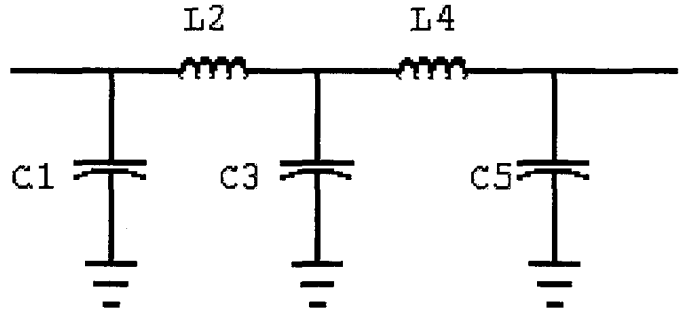

Figure 4.14 5-element Chebyshev low-pass filter

The filter's designed cut-off frequency is 22MHz; the 3dB attenuation frequency is 25.6MHz; the 20dB attenuation frequency is 34.6MHz; the 40dB attenuation frequency is 51.1MHz [Wolfgang, 2001]. Figure 4.15 presents the attenuation response curve of the implemented filter. The input is a sine wave at 1V peak to peak. The output of the filter is measured by the Tektronix 2445A oscilloscope. Because of the limitation of the oscilloscope, the output beyond 40MHz is too small to be detected. This result proves that the actual filter's performance almost agrees with the design.

4.7 Performance of the Transmitter

In order to test the performance of the transmitter, the DDS board is configured to generate some signals and the outputs of the power amplifier are fed to the Tektronix

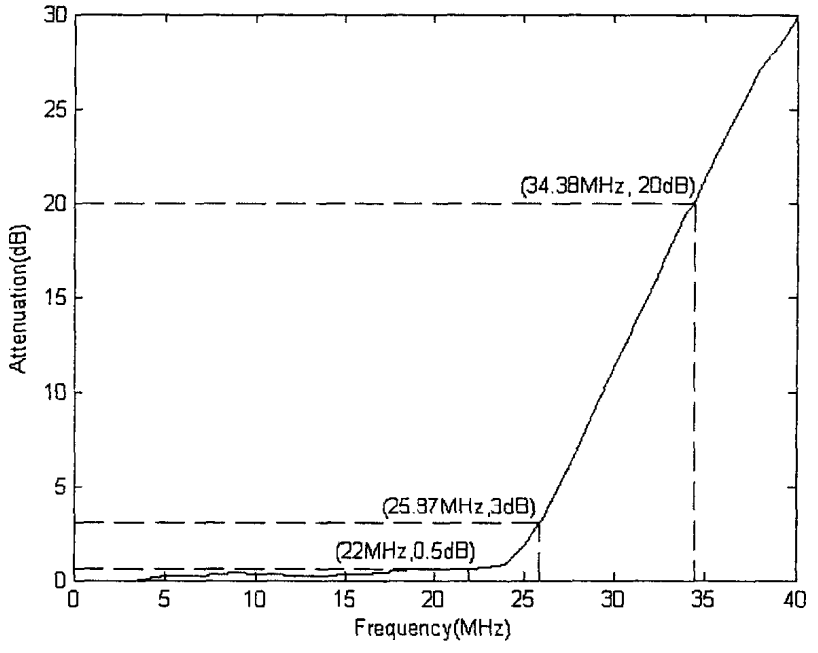

Figure 4.15 Attenuation response curve of the Chebyshev low-pass filter

2445A oscilloscope and the HP 8590A spectrum analyzer. As the output of the transmitter is too big for the oscilloscope and spectrum analyzer, a 40dB attenuator is placed after the power amplifier.

Figure 4.16 shows the output of the power amplifier with a sine wave at 18MHz generated by the DDS board. Figure 4.16(a) and (c) show the output before the filter. As expected, odd-order harmonics are very strong: the third harmonic (54MHz) is less than 10dB below the 18MHz signal and the fifth harmonic (90MHz) is around 25dB below. While the even-order harmonics—36MHz and 72MHz—are around 35dB below. Figure 4.16(b) and (d) illustrate the output after the filter. All the harmonics are 40dB below the fundamental 18MHz signal and the signal shows no distortion.

Figure 4.17 shows the output after the filter with two sine waves at 18MHz and 17.985MHz coming from the DDS board. Figure 4.17(a) shows that all the harmonics are very small. At 36MHz, there is a small peak which is around 35dB below the signal.

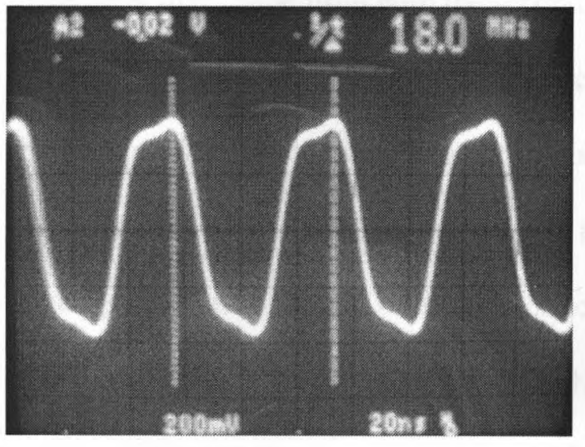

(a) Output before the filter

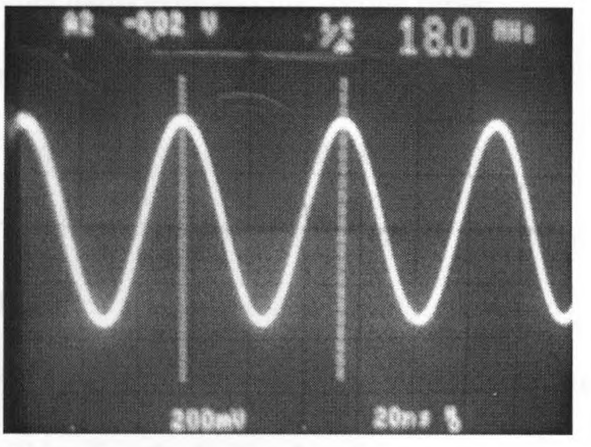

(b) Output after the filter

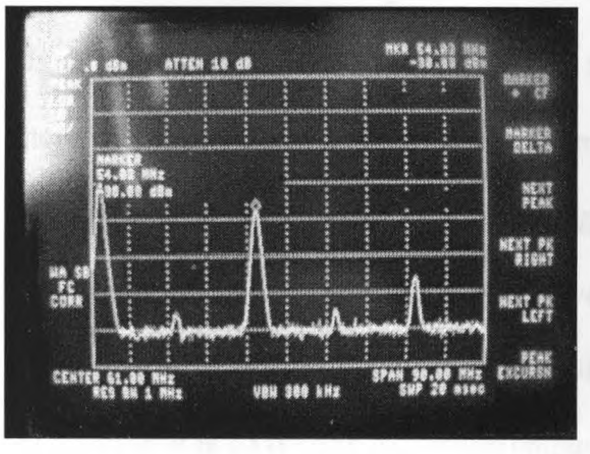

(c) Spectrum of output before filter

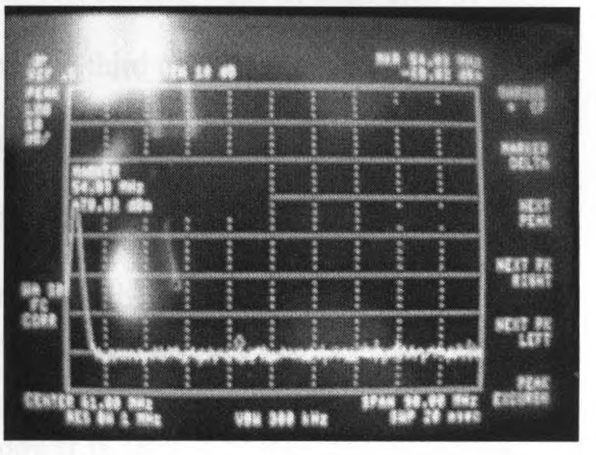

(d) Spectrum of output after filter

Figure 4.16 Power amplifier output of an 18MHz sine wave

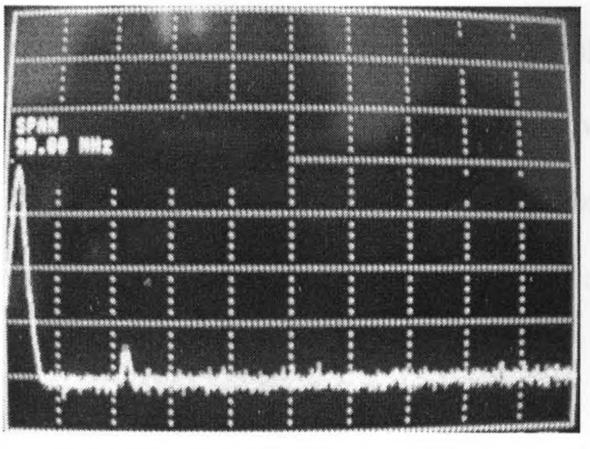

(a) Spectrum: 16MHz to 106MHz

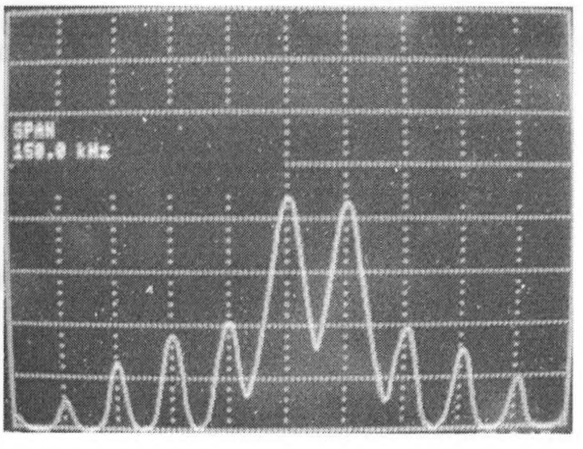

(b) Spectrum: 17.910MHz to 18.060MHz

Figure 4.17 Power amplifier output of 18MHz and 17.985MHz sine waves

This peak may come from both the second order harmonics and the second order intermodulation. Figure 4.17(b) shows intermodulation distortions in the output. The biggest intermodulation components are the two third order intermodulations—17.970MHz and 18.015MHz— which are around 25dB below the two signals. It usually takes great effort to get rid of these intermodulations at the transmitting side. As Wang states in her thesis [Wang, 2006], the bandwidth of the RRI receiver on e-POP is variable up to 30KHz; the signals collected by RRI will be directly digitized at the speed about 40MHz, and then the two signals--18MHz and 17.985MHz-- can be separated by digital signal processing. So the worst case is that the two third order intermodulations are included in the signals. However, in the same way, the intermodulation components can be separated from the desired signals by digital signal processing.

Figure 4.18 illustrates the output power versus the frequency. This transmitter works at 4MHz when it is tested with CADI. At 4MHz, the transmitting power is 34W. At 18MHz, it is 15W. The maximum output power is 38W at 1MHz. The minimum output power is 12W at 20MHz. When the 18MHz and the 17.985MHz signals are generated at the same time, the output power of them are both at around 7W. This can satisfy the power level requirement of e-POP mission. The output power at 8MHz frequency is quite low, because the distortion at that frequency is very severe. This transmitter is not designed to work at 8MHz. If it is required to work at 8MHz in the future, adding a low-pass filter in this band can solve the problem.

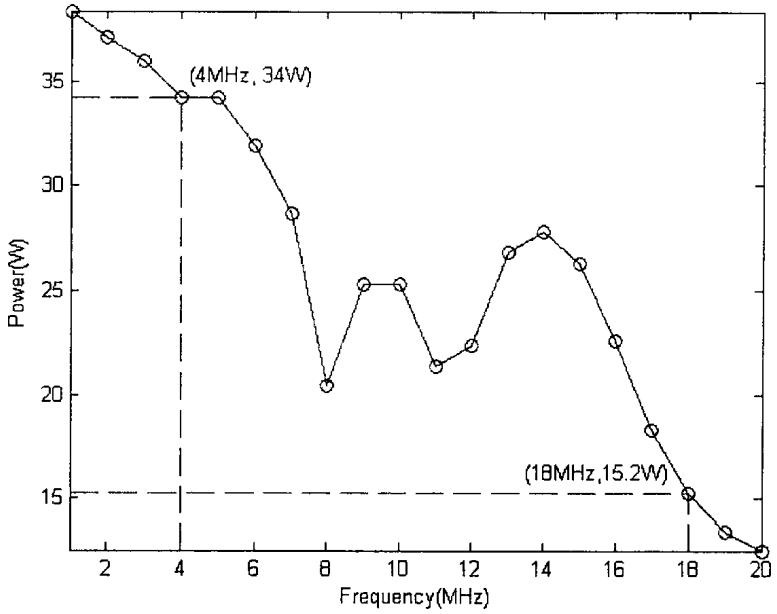

Figure 4.18 Power amplifier output power versus frequency

Chapter 5. The Experimental Setup and Results

In order to test the transmitters, three of them are deployed to detect the ionosphere and measure the TIDs in the ionosphere.

5.1 Experimental Setup

As introduced in Chapter 2, at least three transmitters are required to measure the TIDs in the ionosphere. In the field experiments, three transmitters are set up at Walsingham (42°38'16"N,80°34'21"W), Delaware (42°51'0"N,81°28'48"W), and Tavistock (43°18'36"N, 80°43'52"W). A CADI radar on the UWO campus (43°0'35"N, 81°16'20"W) operates as a receiver to collect signals coming from these three transmitters. If the direction from Delaware to Walsingham is regarded as X axis, and the direction perpendicular to that is regarded as Y axis, Figure 5.1 can be obtained. From

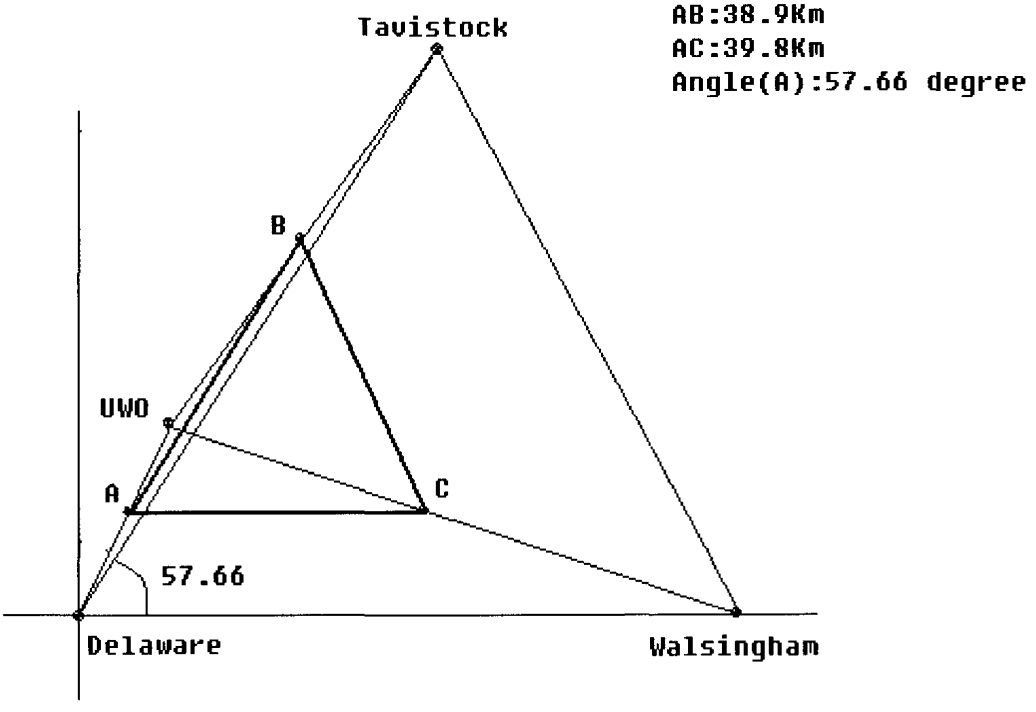

Figure 5.1 Locations of the field experimental transmitters and receiver setup

radio propagation theory, we know that the signal from Delaware received by the CADI is reflected at the middle point, A. The same is with B and C. So the real measured ionosphere locations are at A, B, and C. If A is chosen as the origin point, Figure 2.4 can be obtained. Following the method illustrated in Chapter 2, the speed and direction of the TIDs can be calculated by measuring the time delay between A and C, and between A and B.

Figure 5.2 shows the timing diagram of the field experiment. The transmitters and receiver are synchronized by the GPS PPS signal every second. In order to be separated from others, each transmitter transmits in a fixed time slot. Since CADI can be configured to receive signals every 50ms, and each transmitter just needs to transmit once per second, a time schedule, different from that for e-POP mission which is illustrated in Chapter 4, is used. In this experiment, transmitters at Walsingham, Delaware, and Tavistock are set to start transmitting at the time PPS signal arrives, 100ms after PPS signal arrives, and 200ms after, respectively. The longest propagation path is from Walsingham to UWO, which is 70.5km long. Assuming the F2 region is at 400km, it takes the signal 2.7ms to travel from the transmitter to the receiver. So the 100ms delay between transmitters is long enough that the signal from one transmitter can be reflected by the ionosphere and arrive at the receiver long before the next one starts transmitting.

Each transmitter transmits a LS113 sequence and works at 4MHz. For each of them, a half wavelength dipole antenna is employed. The length L of the dipoles can be calculated by the following equation. [ARRL handbook, 1991]

$$L(\text{ft}) = \frac{492 \times 0.95}{f(MHz)} = \frac{468}{f(MHz)} \qquad \textbf{(5.1)}$$

For 4MHz, the length is 117 feet or 35.662 meters.

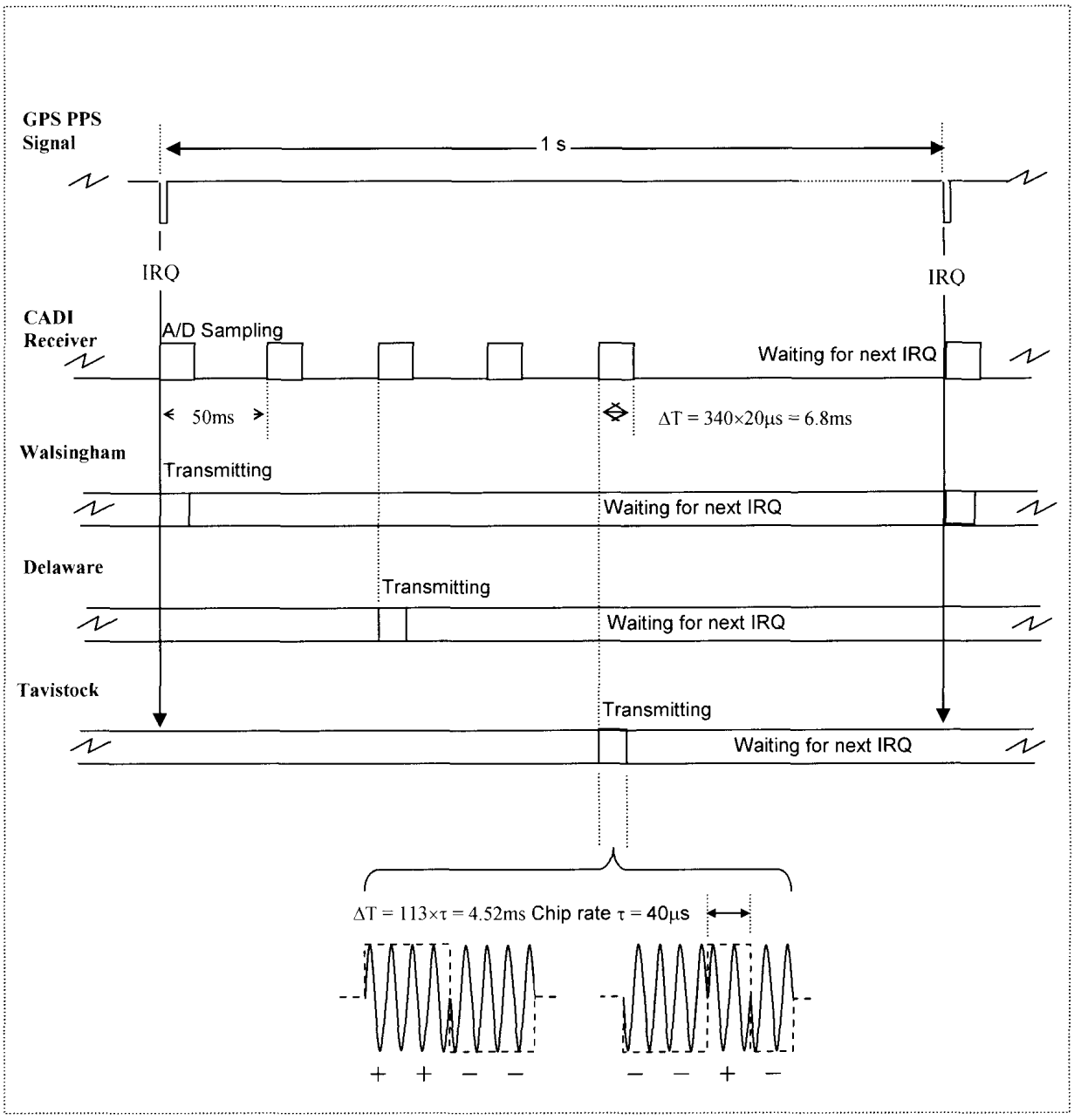

Figure 5.2 Timing diagram of the field experiment system

5.2 Lab Experiments

Before field experiments, the transmitters were tested in the laboratary. Chapter 4 shows that the output of transmitter can satisfy the signal and power level requirements. As it only takes a few milliseconds for signals to travel from transmitter to receiver,

timing is another important factor. Further experiments were done to make sure the transmitters and the receiver are precisely synchronized.

During the testing, the output from the transmitters is fed directly to the receiver through an attenuator. It is assumed that there is no time delay between the signal being transmitted and being received. Figure 5.3(a) illustrates the results when the transmitters start transmitting at the beginning of their own time slots. The peak locations represent half the distance that the signals travel. So, for this experiment, as shown in the figures, all the main peaks should appear at 0. Next, assuming the signal is reflected by the F region at 330km, all the transmitters are set up to start transmitting 1.1ms after their time slots come. These results are shown in Figure 5.3(b). These two experiments were repeated several times. All the results agreed with the Figure 5.3 and demonstrated that the synchronization between the transmitters and the receiver was correct.

5.3 Field Experiments

5.3.1 Data Analysis

The receiver board in CADI is configured to sample both I and Q channel signals and send them to a PC. The PC records all the data of every one hour in a MD1 file. A Matlab program is written to read the data from the MD1 file, correlate the data with the Legendre 113 code, and save the correlation results in a MAT file. The peaks in the correlation results represent the targets, such as E and F region, and their locations represent the group range or virtual height of the targets. These results are used to generate the virtual height versus time ($h't$) plots. Anther Matlab program is written to show the ($h't$) plots observed from the three transmitters on the PC screen, as shown in Figure 5.4. Users can choose to load data from different times, and set up parameters,

Walsingham Station

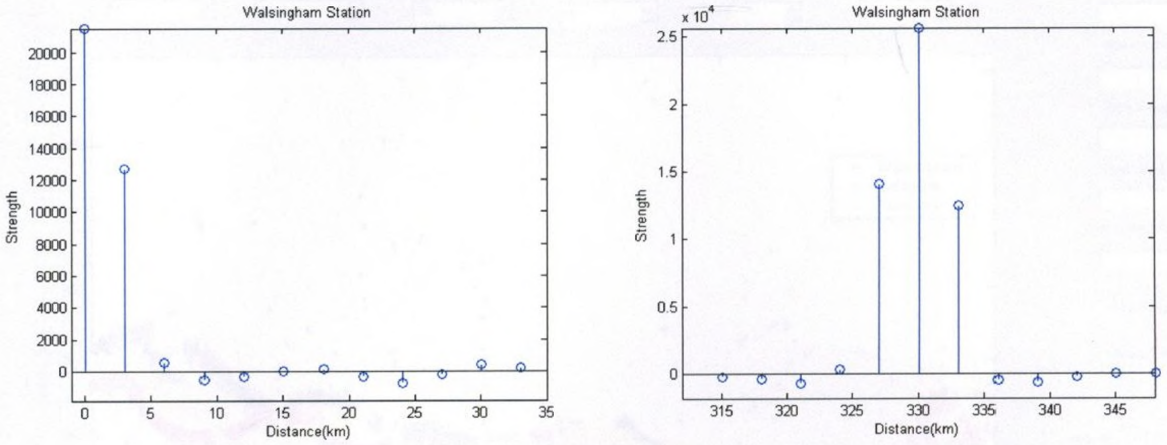

Delaware Station

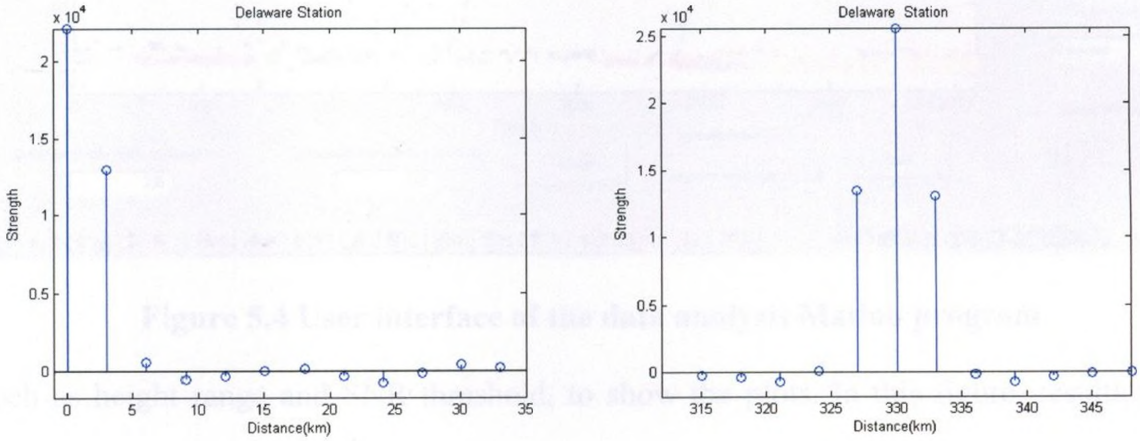

Tavistock Station

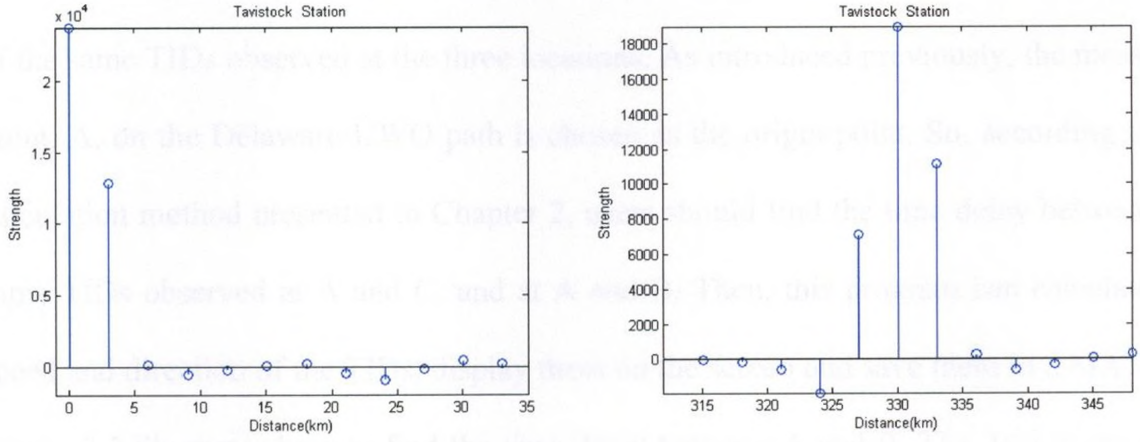

(a) Transmit at the time slot (b) Transmit 1.1ms after the time slot

Figure 5.3 Transmitter synchronization experiments results

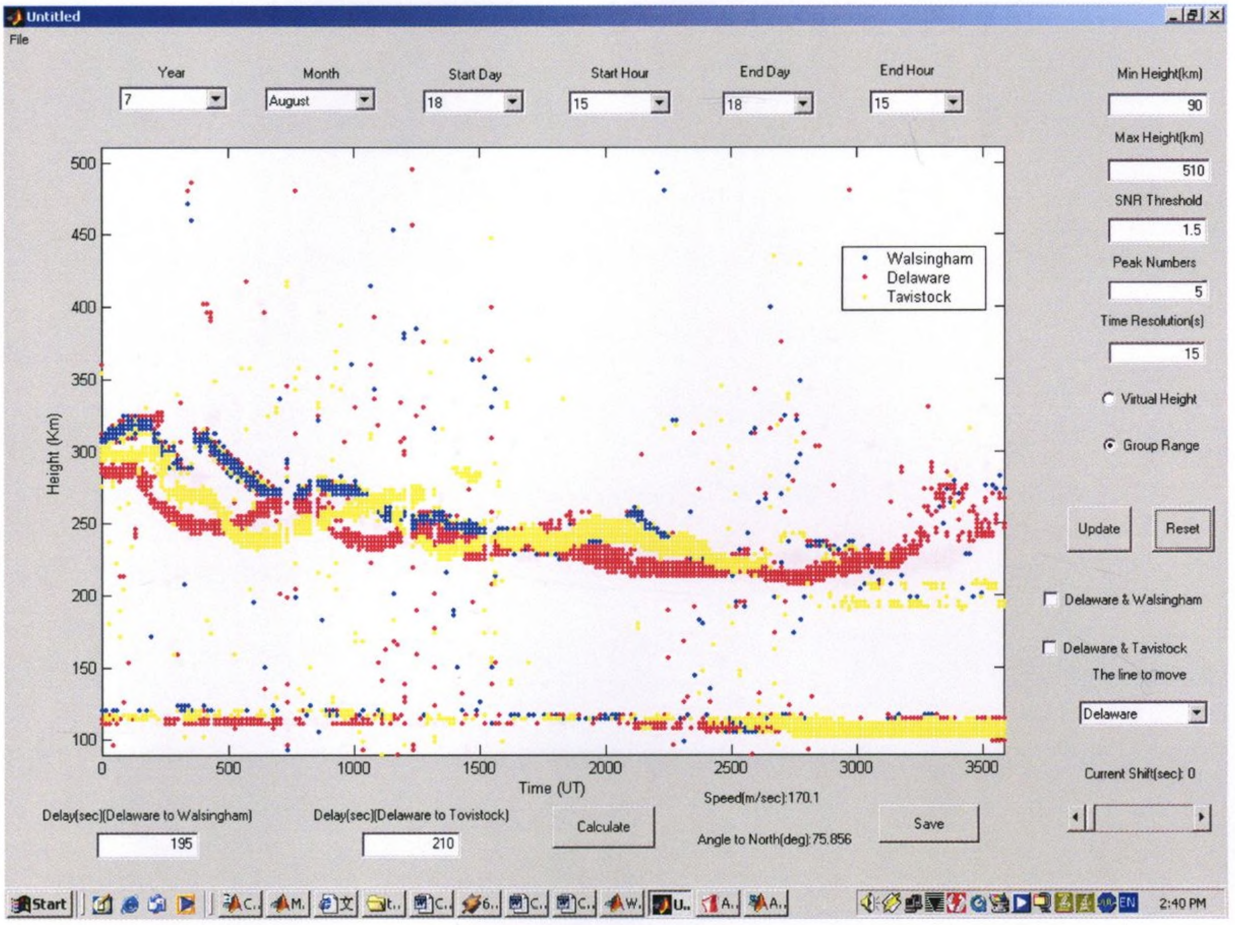

Figure 5.4 User interface of the data analysis Matlab program

such as height range and SNR threshold, to show the plots. In this figure, results from universal time hour 15, August 18th are shown. With the slide bar, this program also allows users to move these traces one at a time along the time axis to find the time delay of the same TIDs observed at the three locations. As introduced previously, the measured point, A, on the Delaware-UWO path is chosen as the origin point. So, according to the calculation method presented in Chapter 2, users should find the time delay between the same TIDs observed at A and C, and at A and B. Then, this program can calculate the speed and direction of the TIDs, display them on the screen and save them in a MAT file. Figure 5.5 illustrates how to find the time delay between A and B. The data is the same with Figure 5.4. In this figure, trace from A on the Delaware-UWO path is moved along

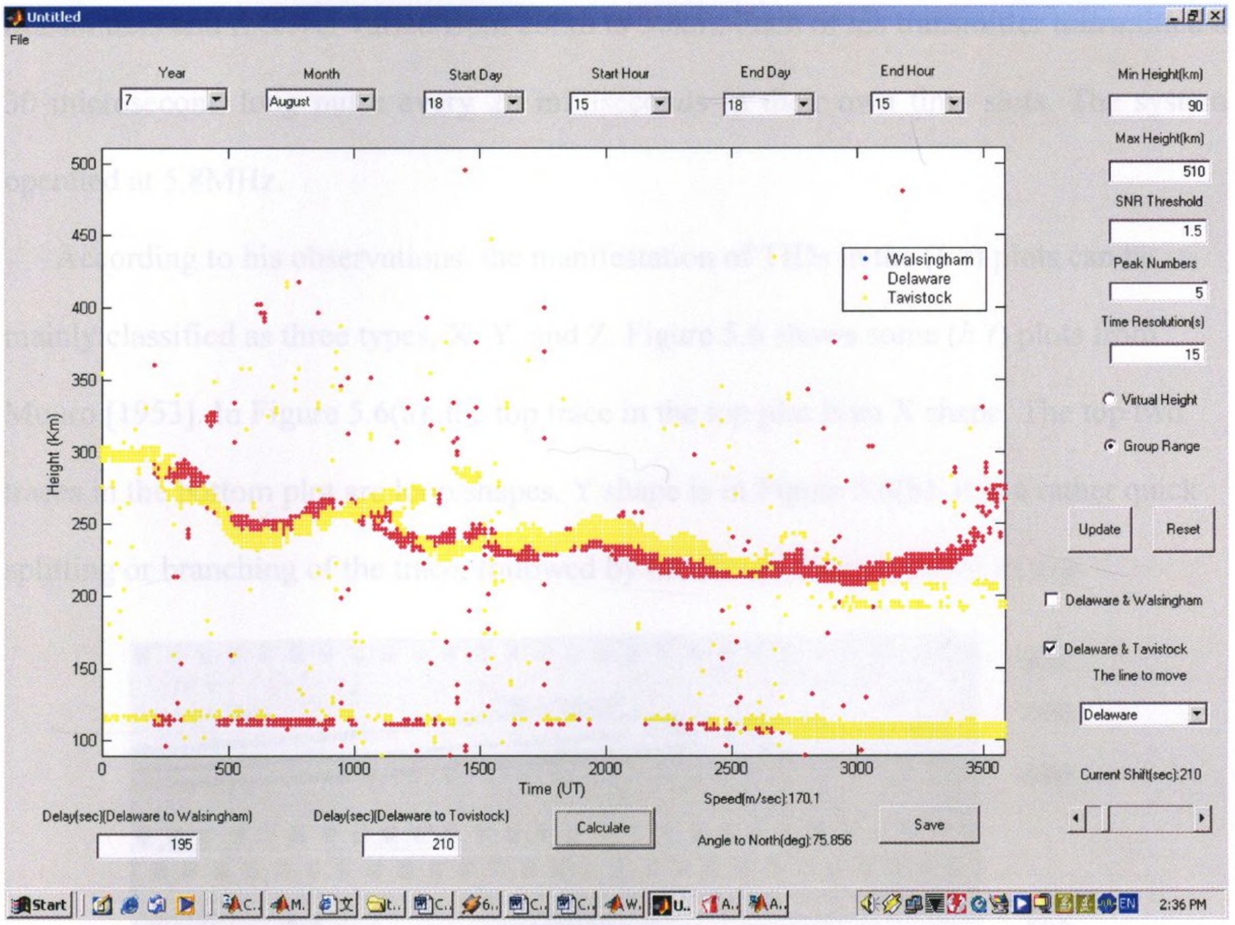

Figure 5.5 User interface for TIDs analysis

the time axis for 210 seconds and agrees well with the trace observed from B on Tavistock-UWO path. So the time delay between these two is 210 seconds. The time delay between A on Delaware-UWO path and C on Walsingham-UWO path can be found to be 195 seconds. Therefore, the speed and direction of the TIDs are 170.1 meter per second and 75.856 degree clockwise from true North.

5.3.2 TIDs Analysis

After obtaining all the data required, the question is how to identify a TID.

Munro [1950, 1953, 1958] measured the TIDs for 9 years from 1948 to 1957. The way we measure TIDs is similar to his. In his research, three transmitters and one receiver were deployed and all of them were synchronized. The distances between

transmitters and receiver varied from 20km to 50km. Each of his transmitter transmitted a 30 microsecond long pulse every 20 milliseconds in their own time slots. The system operated at 5.8MHz.

According to his observations, the manifestation of TIDs in the (*h't*) plots can be mainly classified as three types, X, Y, and Z. Figure 5.6 shows some (*h't*) plots from Munro [1953]. In Figure 5.6(a), the top trace in the top plot is an X shape. The top two traces in the bottom plot are loop shapes. Y shape is in Figure 5.6(b). It is a rather quick splitting or branching of the trace, followed by the abrupt disappearance of one

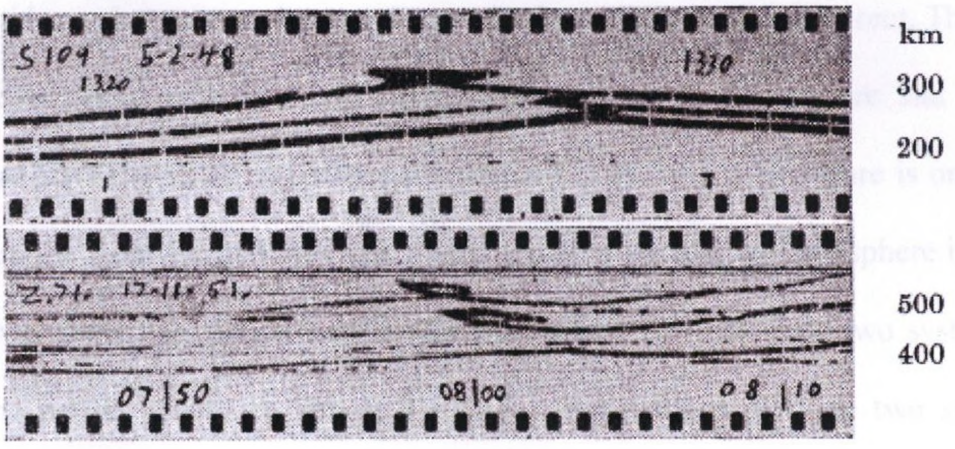

(a) X or loop shape disturbances

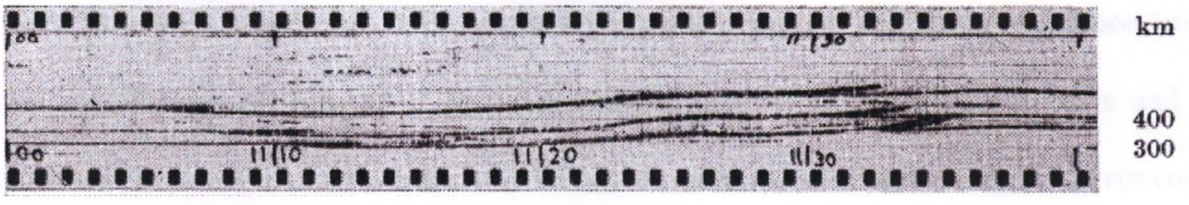

(b) Y shape disturbances

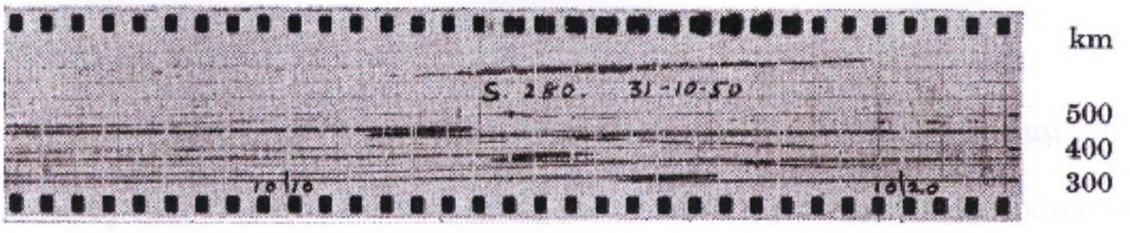

(c) Z shape disturbances

Figure 5.6 Different TIDs shapes on h't plot [Munro, 1953]

branch. Figure 5.6(c) shows Z shape. If these three types are not available, TIDs can also be identified by virtual height peaks; virtual height dips; and cross-over point of 'o' and 'x' rays [Munro, 1950]. However, they are not as precise or reliable as those three types. The possible reason of the appearance of those three types is given in the paper by Munro [1953].

5.3.3 Results

A. Result from Transmitter at Delaware

A CADI radar is operating at the same site with one of the transmitters at Delaware. This provides a chance to make sure the results from our system are correct. The CADI at Delaware works as a vertical ionosonde. The transmitter at Delaware and the CADI receiver at UWO work as an oblique ionosonde. As the site at Delaware is only 24.5km away from the receiver; and previous observations prove that the ionosphere is quite flat in this area, the virtual height versus time plots obtained from these two systems at the same time period should be almost the same. Observations of these two systems are compared. The comparison demonstrates that the observations from these two systems agree quite well. Figure 5.7 shows an example which is an all day long observation from the two systems on July 15. CADI has been running for more than ten years and is regarded as a reliable ionosonde. So it can be concluded that the field experimental system works correctly.

B. TIDs Observations

The observations of TIDs were implemented from August 17 to August 27. As suggested by Munro [1958], the time resolution of the ($h't$) plot is normally chosen to be 15 seconds, and 30 seconds are used in some cases. TIDs are identified by the X, Y, and

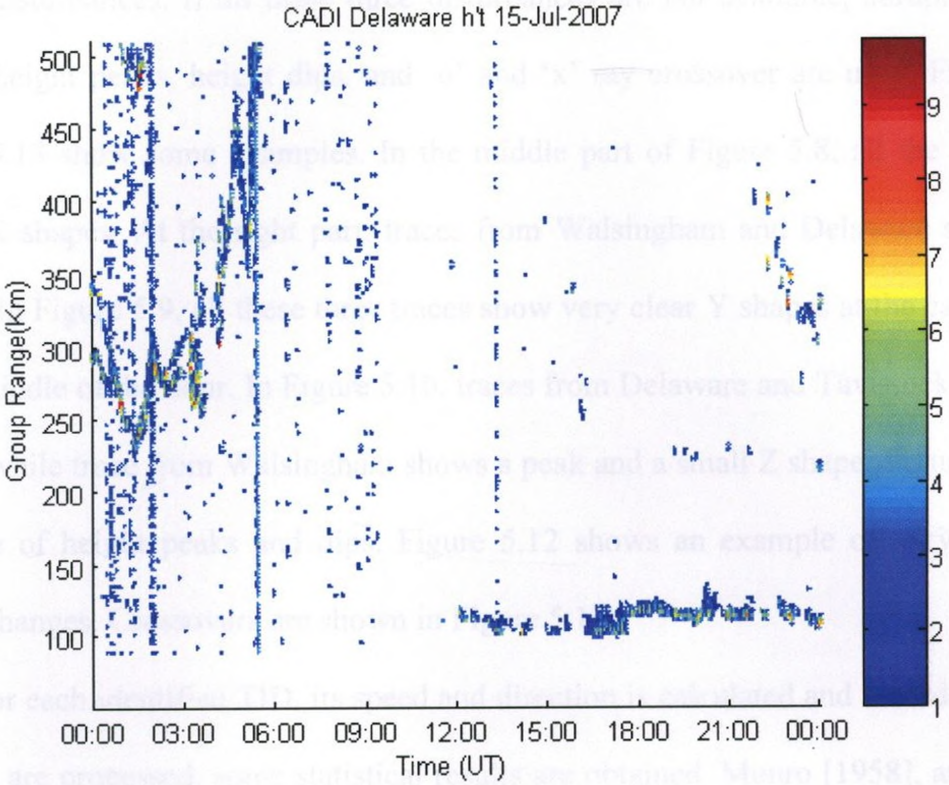

(a) *h't* plot from CADI at Delaware

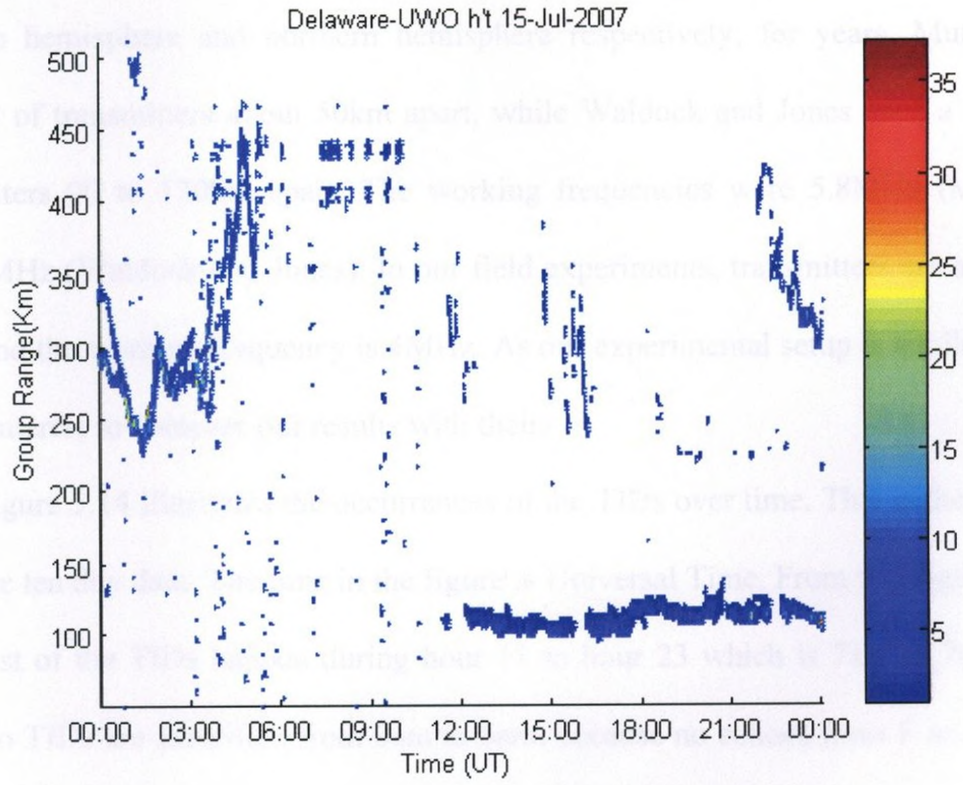

(b) *h't* plot from Transmitter at Delaware and Receiver at UWO

Figure 5.7 *h't* plots from field experiment on July 15th, 2007

Z type disturbances. If all these three disturbances are not available, abrupt changes in height, height peaks, height dips, and 'o' and 'x' ray crossover are used. Figure 5.8 to Figure 5.13 show some examples. In the middle part of Figure 5.8, all the three traces shows X shapes. At the right part, traces from Walsingham and Delaware shows Loop shapes. In Figure 5.9, all these three traces show very clear Y shapes at the early part and in the middle of the hour. In Figure 5.10, traces from Delaware and Tavistock show big Z shapes while trace from Walsingham shows a peak and a small Z shape. Figure 5.11 is an example of height peaks and dips. Figure 5.12 shows an example of very big abrupt height changes. Crossovers are shown in Figure 5.13.

For each identified TID, its speed and direction is calculated and recorded. After all the data are processed, some statistical results are obtained. Munro [1958], and Waldock and Jones [1986] observed TIDs at mid-latitudes with networks of transmitters, at southern hemisphere and northern hemisphere respectively, for years. Munro used a network of transmitters about 50km apart, while Waldock and Jones used a network of transmitters 90 to 120km apart. The working frequencies were 5.8MHz (Munro) and 4.7925MHz (Waldock and Jones). In our field experiments, transmitters are about 80km apart; and the working frequency is 4MHz. As our experimental setup is similar to theirs, it is of interest to compare our results with theirs.

Figure 5.14 illustrates the occurrences of the TIDs over time. This is the sum result of all the ten day data. The time in the figure is Universal Time. From this figure, we find that most of the TIDs happen during hour 11 to hour 23 which is 7am to 7pm in local time. No TIDs are identified from 0am to 6am, because no echoes from F and E regions are received during this period. The total number of TIDs identified is 117. So the

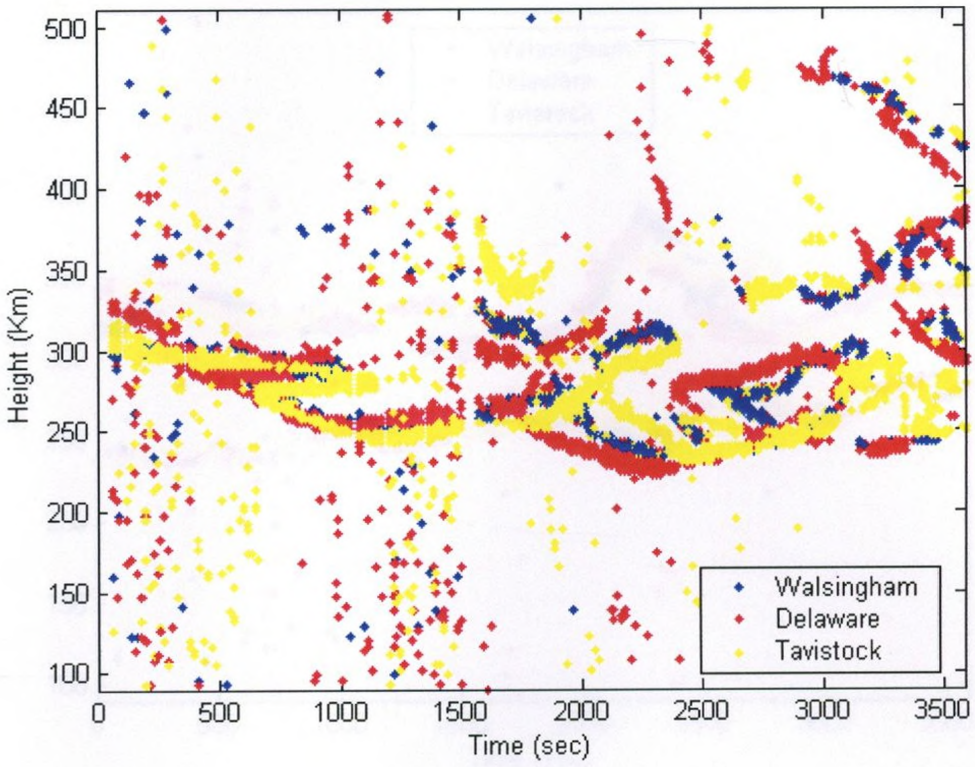

Figure 5.8 Observation of X and Loop type disturbances at hour 11, August 25

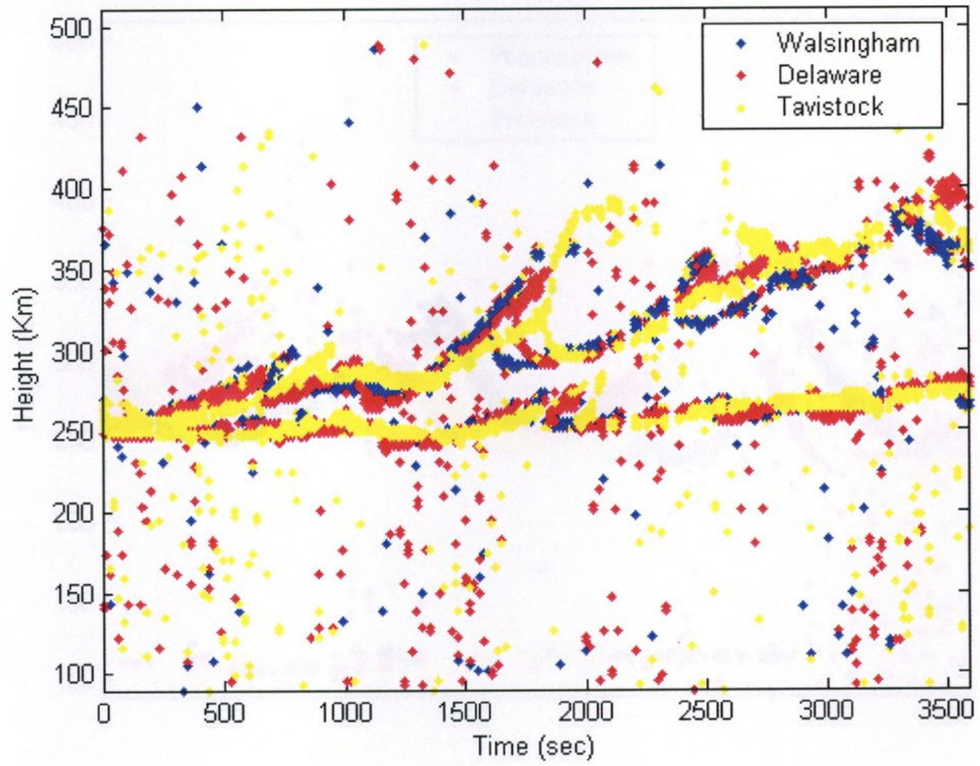

Figure 5.9 Observation of Y type disturbances at hour 0, August 17

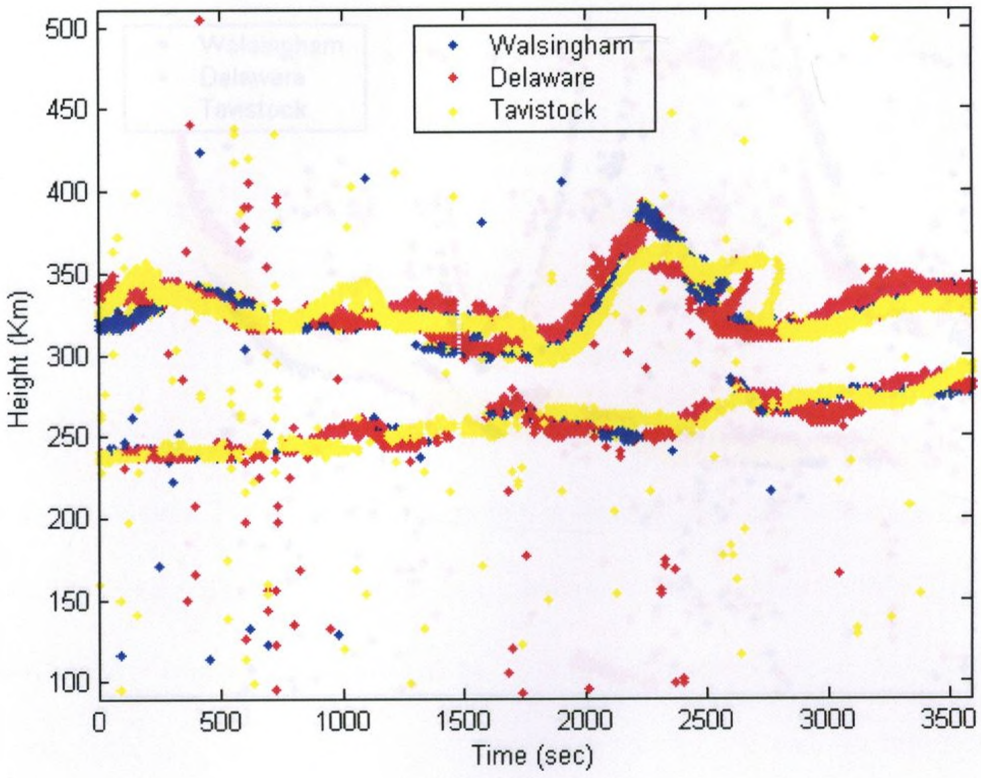

Figure 5.10 Observation of Z type disturbances at hour 22, August 17

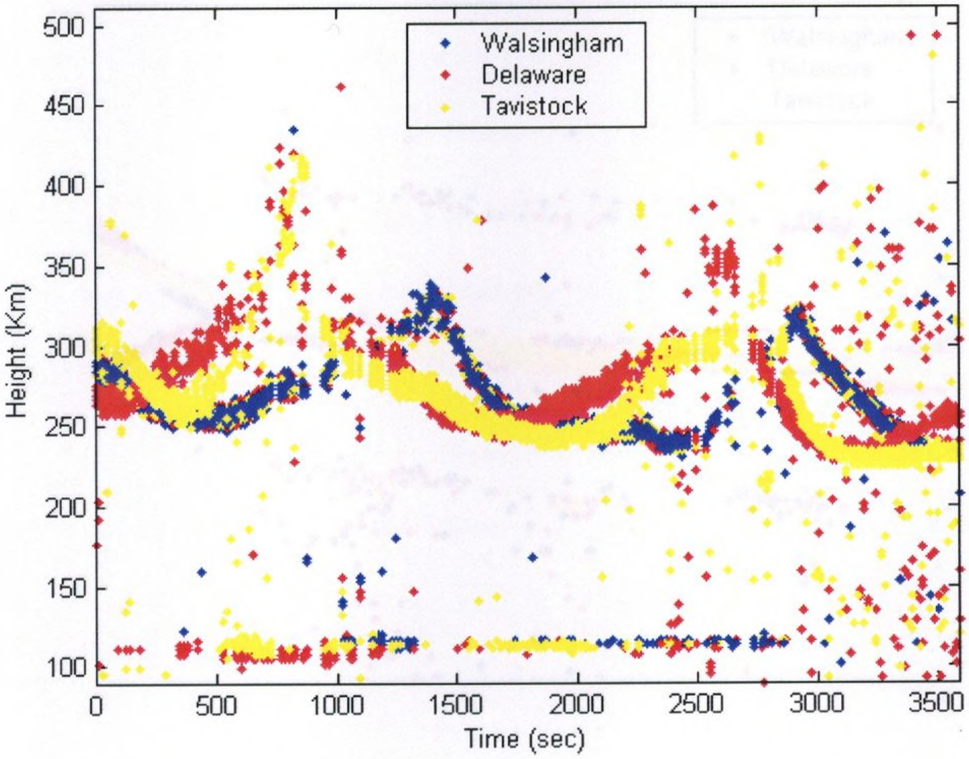

Figure 5.11 Observation of peaks and dips at hour 15, August 17

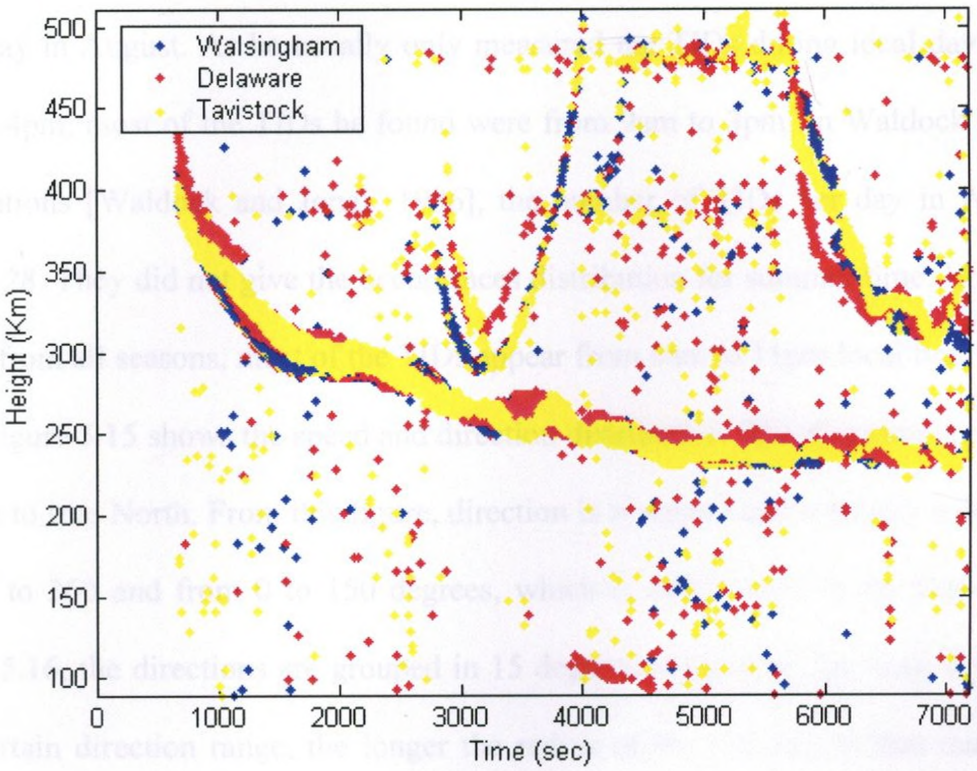

Figure 5.12 Observations of abrupt changes at hour 11-12, August 21

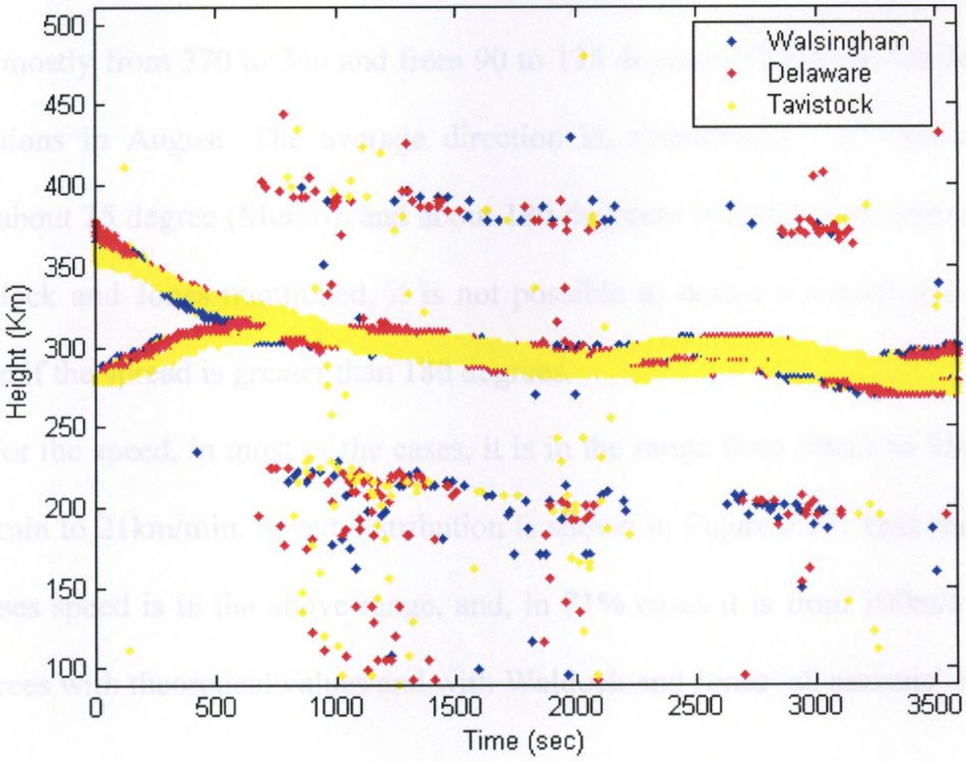

Figure 5.13 Observations of crossover at hour 23, August 18

average occurrence per day is 12. In Munro' result [Munro, 1958], the occurrences rate is 7 per day in August. As he usually only measured the TIDs during local daytime, from 8am to 4pm, most of the TIDs he found were from 9am to 3pm. In Waldock and Jones' observations [Waldock and Jones, 1986], the number of TIDs per day in August was around 28. They did not give the occurrences distribution for summer time. However, for results from all seasons, most of the TIDs appear from 6am to 11pm local time.

Figure 5.15 shows the speed and direction distribution. The direction is the azimuth relative to true North. From this figure, direction is scattered and normally is in the range of 330 to 360 and from 0 to 150 degrees, which is also shown in the Figure 5.16. In Figure 5.16, the directions are grouped in 15 degrees segments. The more TIDs moving in a certain direction range, the longer the radius of the red area in that range is. The result shows that most of the TIDs go eastward and poleward, which agrees with Munro's (mostly from 0 to 80 and from 330 to 360 degrees) [Munro, 1958] and Waldock and Jones' (mostly from 270 to 360 and from 90 to 135 degrees) [Waldock and Jones, 1986] observations in August. The average direction is, respectively, 133 degrees (present study), about 25 degree (Munro), and about 180 degrees (Waldock and Jones). However, as Waldock and Jones mentioned, it is not possible to derive a meaningful average of direction if the spread is greater than 180 degrees.

For the speed, in most of the cases, it is in the range from 50m/s to 350m/s which is 3km/min to 21km/min. Speed distribution is shown in Figure 5.17. This shows that, in 97% cases speed is in the above range, and, in 71% cases it is from 100m/s to 250m/s. This agrees with theoretical values and with Waldock and Jones' all seasons' observation

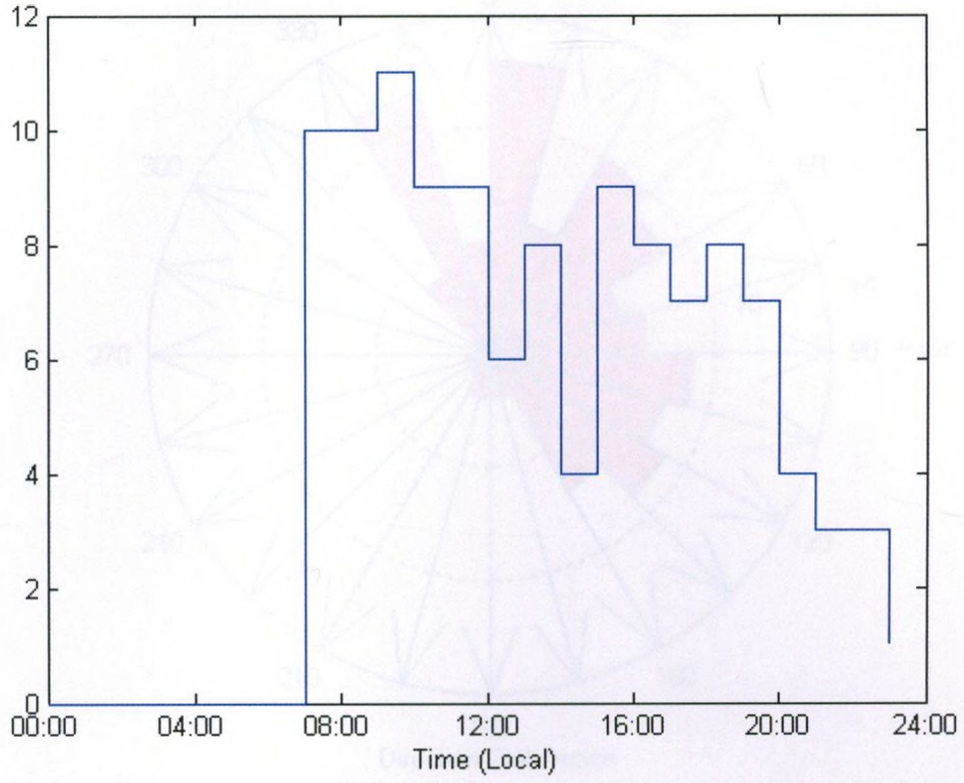

Figure 5.14 Occurrences distribution of TIDs over time

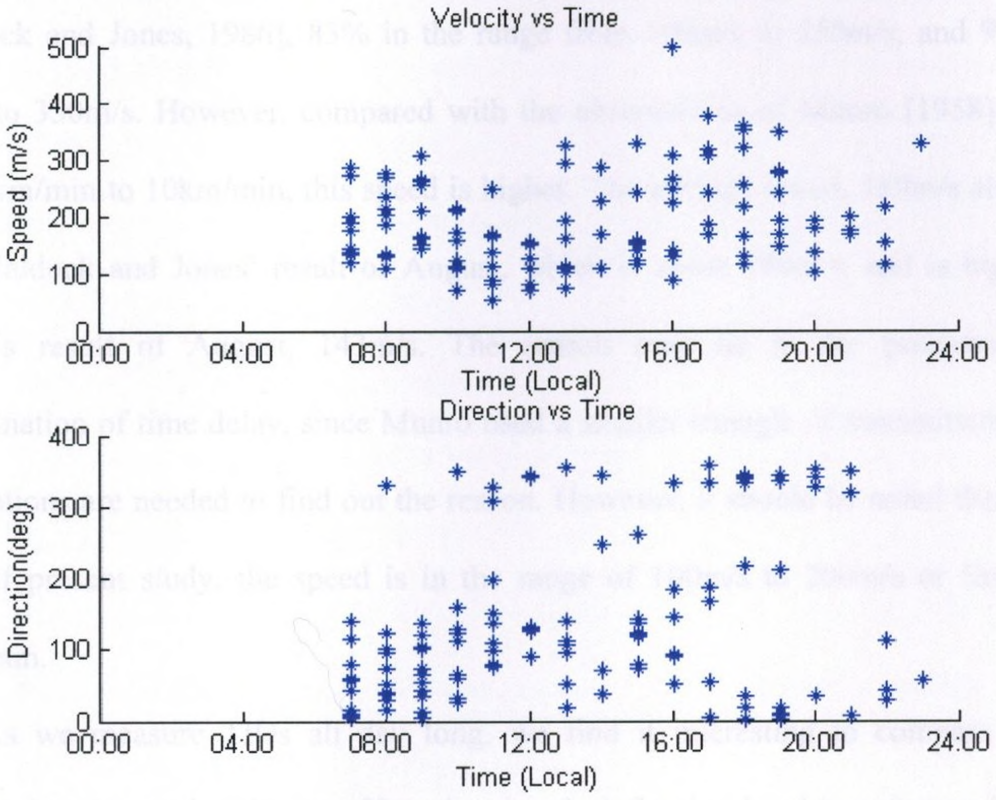

Figure 5.15 TIDs speed and direction distribution over time

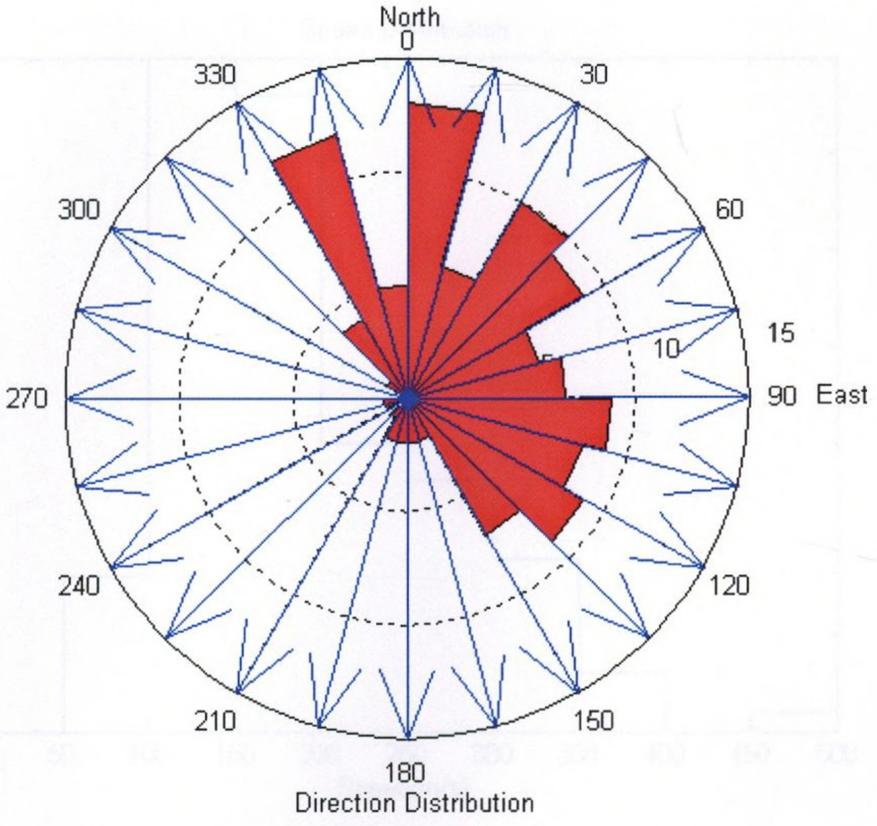

Figure 5.16 TIDs moving direction distribution

[Waldock and Jones, 1986], 83% in the range from 100m/s to 250m/s, and 97% from 50m/s to 350m/s. However, compared with the observations of Munro [1958]—mostly from 5km/min to 10km/min, this speed is higher. The average speed, 189m/s also agrees with Waldock and Jones' result of August, which is about 180m/s, and is higher than Munro's result of August, 143m/s. The reason may lie in the precision of the determination of time delay, since Munro used a smaller triangle of transmitters. Further observations are needed to find out the reason. However, it should be noted that, in 58% cases of present study, the speed is in the range of 100m/s to 200m/s or 5km/min to 12km/min.

As we measure TIDs all day long, we find it interesting to compare the data between day time and night time. Here day time is defined as local time 6am to 5pm.

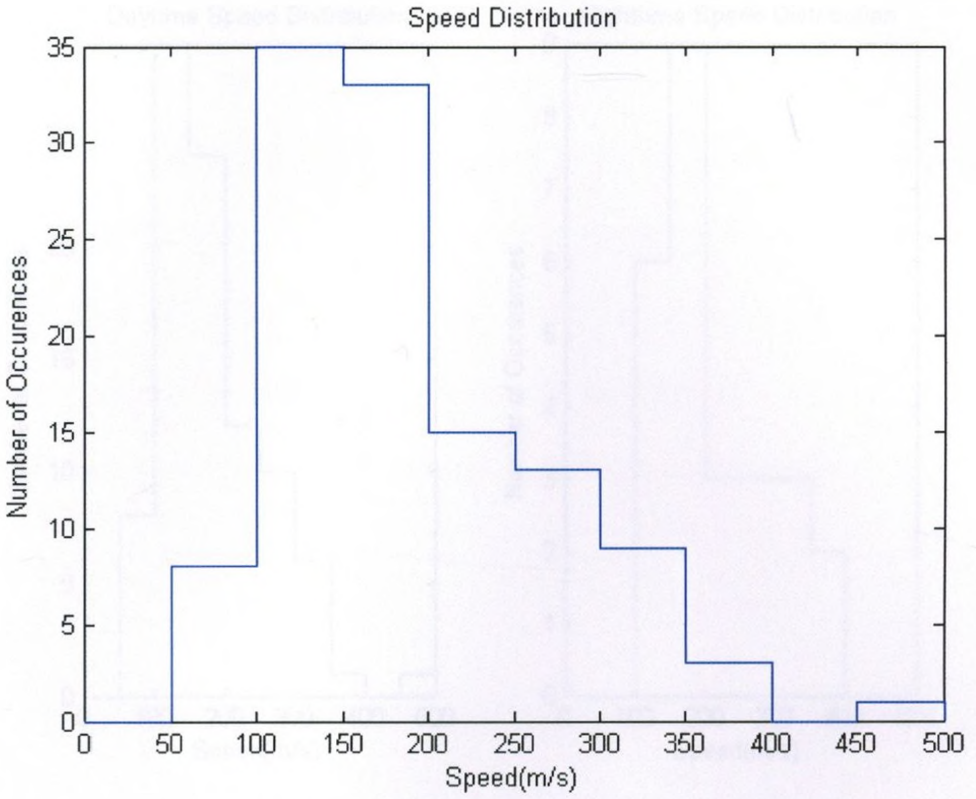

Figure 5.17 TIDs moving speed distribution

Night time is from local time 6pm to 5am. Figure 5.18 illustrates the speed distribution difference. At night, speed is restricted to the range from 100m/s to 400m/s. During the day, speed distribution is more scattered. Also, night time speed is higher than day time. The average speed at night time is 213m/s while it is 182m/s during day time. Waldock and Jones' results [Waldock and Jones, 1986] also show that speed increases toward evening hours. They believed that this was probably a consequence of the increased reflection height of the probing radio wave at night. At higher altitude there is more probability that faster and larger scale TIDs can propagate than at lower ionosphere height. This may also explain why the speed result of Munro's is lower, because all his data are from day time. Munro [1958] also measured TIDs in winter night time, 10pm to 2am local time, but only for 22 nights in June 1953. His nighttime results also show higher velocities than during day time.

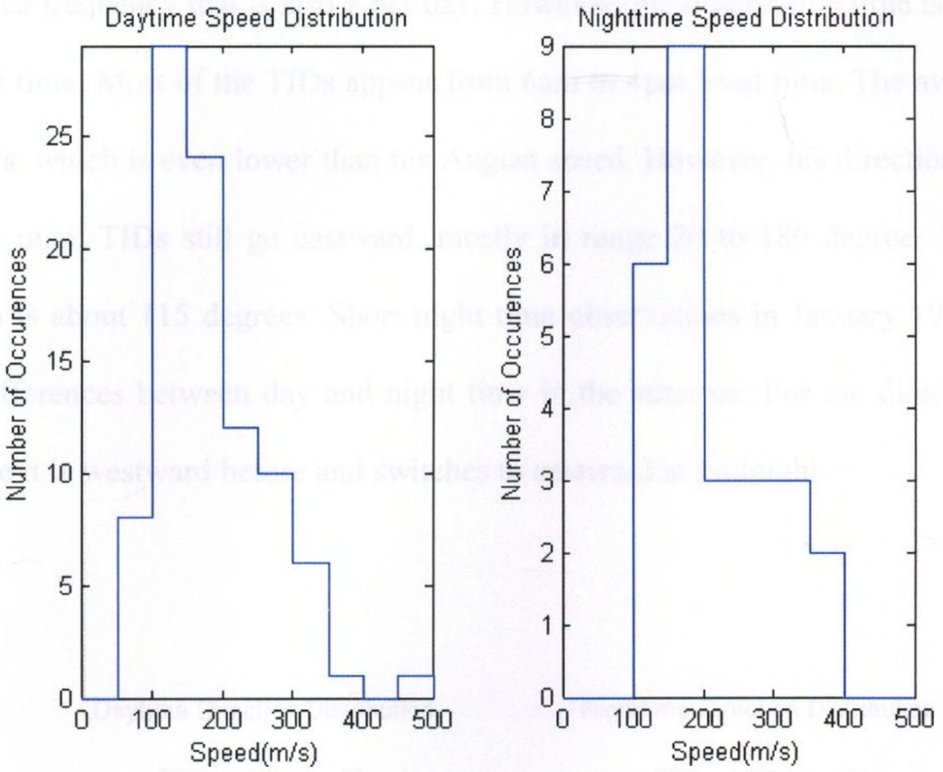

Figure 5.18 Comparison of TIDs speed distribution between daytime and nighttime

Figure 5.19 shows the direction distribution of day time and night time. During the day, most of the TIDs go eastward. At night, almost all the TIDs go northward. This agrees with both Munro's August [Munro, 1958] and Waldock and Jones' all seasons results [Waldock and Jones, 1986], both of which are mostly eastward during day time and are in the west-north quadrant at night time. To explain this, Waldock and Jones suggest that, because of the filtering action of neutral winds, the propagation direction of TIDs should rotate clockwise by 360 degrees in 24 hours due to daily variations of the neutral winds. They gave an example (their Figure 10) of such a rotation of TID azimuth. However, there is not a smooth rotation, and, as in Figure 5.15, our present data shows similar behavior to theirs.

As August is in winter at southern hemisphere, it is of interest to compare our results with Munro's [1958] summer results. Using January, his result shows an

occurrence frequency that is also 7 per day. However, the observation time is longer than in winter time. Most of the TIDs appear from 6am to 4pm local time. The average speed is 125m/s, which is even lower than his August speed. However, his direction results are closer to ours. TIDs still go eastward, mostly in range 20 to 180 degree. The average direction is about 115 degrees. Short night time observations in January 1957 show no speed differences between day and night time in the summer. For the direction, during nighttime it is westward before and switches to eastward at midnight.

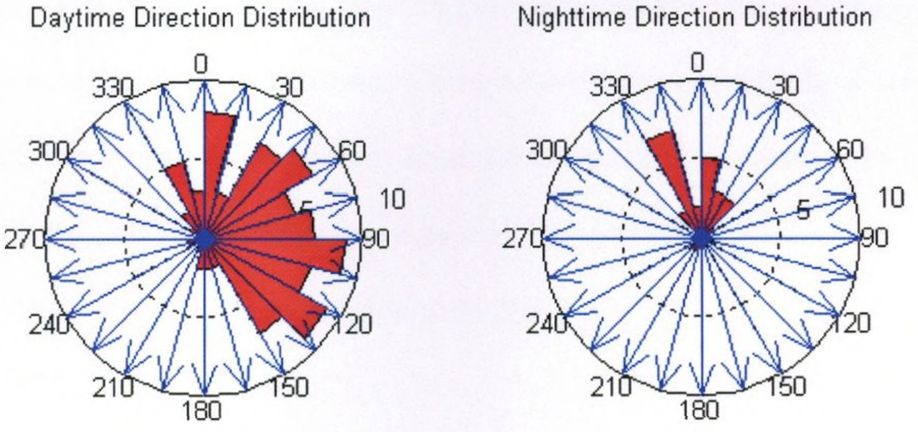

Figure 5.19 Comparison of TIDs direction distribution between daytime and nighttime

From the above analysis, we know that our result agrees quite well with Waldock and Jones' but shows marked difference with Munro's. As we only take 10 days data but Munro measured the TIDs for 9 years, it is too early to give the reasons. More

observations are required. However, the experimental results demonstrate that these transmitters work correctly and can satisfy the e-POP mission requirements. Among the three transmitters, the one at Delaware and the one at Walsingham have been working continuously for over 2 months, which proves that the transmitters are reliable.

Chapter 6. Conclusion and Recommendations

6.1 Conclusion

A dual frequency transmitter for e-POP mission has been developed. It is required to transmit two pulsed adjacent frequency signals in the HF band and work synchronously with each other. The transmitter developed is controlled by a Motorola 9S12 microcontroller and it allows users to set up the parameters through input switch panels. The transmitter can be configured to generate two pulsed adjacent frequency signals, and their phases can be modulated by several different modulation codes, such as Barker 13 and Legendre 113. Lab experiments have demonstrated that the transmitter can operate in the HF band from 1 MHz to 20MHz; the output power level range is from 38W at 1MHz to 12W at 20MHz. Experiment results also show that the transmitter can generate the two signals properly at the same time.

The transmitter is implemented with a CADI radar receiver to detect the ionosphere. The results agree with those obtained from CADI radar system, which proves that the transmitter operates correctly and can work with the CADI radar receiver.

To test these transmitters, three of them and a CADI receiver were synchronized to operate together to measure the TIDs in the ionosphere. This field experiment achieved success and proves the ability of the transmitters to operate synchronously with others. Two of the transmitters have been running for over two months, which demonstrates the transmitter's reliability.

The observations of TIDs are compared with the results of other researchers. The

results show that, in summer time, at mid-latitude, most medium-scale TIDs move at the speed of 100m/s to 300m/s; most of them move eastward during day time and poleward during night time; and TIDs move faster during night time than during day time.

6.2 Recommendations

6.2.1 The Oscillator

On the DDS board, an oscillator is used to provide the reference clock to the DDS chip. As illustrated in Chapter 4, the output frequency of the DDS chip is proportional to the reference clock. Therefore, if the actual reference frequency is off the nominal value, the output frequency will also be off the required value.

The frequency tolerance of the oscillator utilized in this design is ±100ppm, which means the error of the oscillator is in the range of ±100Hz per mega-Hertz. The nominal value of the oscillator is 64.000000MHz. However, the real output as measured varies from 63.999670 to 63.999850 MHz. For the oscillator with 63.999670MHz output, the actual 4MHz and 18MHz outputs of the DDS chip are around 3.999980MHz and 17.999910MHz.

This frequency error does not affect the range or location detection of the targets [Jing, 2003]. As only height information is used in our TIDs observations, it does not introduce errors to the results. However, if Doppler shift information is required from the echoes received by the receiver, errors will be introduced. The relation of Doppler shift, f_d, and radial velocity, v_d, of targets along the line sight of the radar to the targets is:

$$f_d = \frac{2v_d}{\lambda} \tag{6.1}$$

where λ is the wavelength of the probing frequency. Suppose the F region is at a height of 400km, the 3.999980MHz signal that propagates along the Walsingham-UWO path, which is 70.5km long, will introduce a 20Hz Doppler shift or 750m/s speed error in the radial direction. This will give a 2270m/s horizontal speed error or 795m/s vertical speed error. Obviously, more stable and precise oscillators are required to avoid these big errors if Doppler or speed information is desired from the echoes.

6.2.2 The pre-Amplifier

The pre-amplifier utilized is the ZHL-32A from Mini-circuit. Its frequency range is 0.05 to 130MHz; the maximum power output is 800mW. However, even with no signal input, it consumes 0.5A at 24V. This makes a high output demand on the power supply. Currently, power supplies with over 1.5A output are used. These power supplies are big and expensive. Another problem of the pre-amplifier is that, since it consumes high current, it generates so much heat that an electric fan is required. In order to make the transmitter more compact and cheaper, a low-current amplifier is preferred.

6.2.3 Observations of TIDs

A network of three transmitters is used to measure the TIDs. However, the experiments are only 10 days long. Although the results obtained partly agree with those obtained by other researchers, there are still some discrepancies. More data are required to find out the reasons for the difference. Moreover, in order to get meaningful statistical results, such as the seasonal variations, longer observations are needed. Because the TIDs and time delay between measured points are identified manually, errors are inevitably introduced. Longer observations can decrease the random errors and therefore obtain more precise speed and direction results.

Another way to decrease the errors is to put up another transmitter and use the data from that transmitter to verify the results obtained from the three transmitters [Waldock and Jones, 1986]. This fourth transmitter can provide valuable redundancy. If the results from these four transmitters agree closely, it will make the results more confident.

APPENDICES

Programs Used for This Project:

A: 9S12dds9851board1~5.asm

These five files are the control programs in the microcontrollers on the five transmitters. These programs are written in Assembly language.

B: readhourmd1.m

The CADI receiver records every one hour data in a MD1 file. This Matlab program reads in data in one MD1 file and saves them in a Matlab data format file.

C: GetHourDatawaldeltav5sec.m

This Matlab program uses B program to read in data of transmitters at Walsingham, Delaware, and Tavistock, correlates them with Legendre 113 code, and saves every five-second data in a Matlab data format file. The period of the data can be specified by the users.

D: GetHourDatawaldeltav5secload.m

This program is the same with C program except that it loads raw data from files saved by B program instead of reading them from MD1 file.

E: GetGraphWalDelTavloadGUI5sec.m

This program reads in data saved by C or D program, extracts data that are in specified height range and above specified SNR ratio, groups them in specified time resolution, such as 10, 15 seconds, etc, and outputs the results in matrix format.

F: WalDelTav15secs.m

This program controls the interface shown in Figure5.4. It uses E program to get the data. Its function is illustrated in Chapter 5.

REFERENCE

Analog Device Inc., *CMOS, 180MHz DDS/DAC Synthesizer*, Norwood, U.S.A, 2004

Davies, K., *Ionospheric Radio Waves*, Blaisdell publishing Company, 1969

Davies, K., *Ionospheric Radio*, Peter Peregrinus Ltd., 1990

EOPORTAL
http://directory.eoportal.org/info_CASSIOPECascadeSmallSatandIonosphericPolarExplorer.html, 2006

Francis, S.H., A theory of medium-scale traveling ionosphere disturbance, *Journal of Geophysical Research*, Vol 79, pp.5245-5260, December 1974

Francis, S.H., Global propagation of atmospheric gravity waves: A review, *Journal of Atmospheric and Terrestrial Physics*, Vol 37, pp. 1011-1054, 1975

Gao, S. X., A pulse compression ionospheric radar, M.S. thesis, Dept. of Elect. Eng., University of Western Ontario, 1991

Georges, T.M., HF Doppler studies of traveling ionospheric disturbances, *Journal of Atmospheric and Terrestrial Physics*, Vol. 30, pp. 735-746, 1968

Huang, J., Pulse coding for ionospheric radar, M.S. thesis, Dept. of Elect. Eng., University of Western Ontario, 2003

Hunsucker, R.D., Hargreaves, J.K., *The High-Latitude Ionosphere and Its Effects on Radio Propagation*, Cambridge University Press, 2003

Jian, W., High resolution ionospheric radar, M.S. thesis, Dept. of Elect. Eng., University of Western Ontario, 1996

Levanon, N., *Radar Signals*, John Wiley & Sons, 2004

Liu, W., et al., Multiscale geospace physics in Canada, *Conference on Sun-Earth Connection: Multiscale Coupling in Sun-Earth Processes.*, edited by A.T.Y. Lui and Y Kamide, Hawaii, 2004

MacDougall, J.W., G. E. Hall, and K. Hayashi, F region gravity waves in the central polar cap, *Journal of Geophysical Research*, Vol. 102, No. A7, pp.14,513–14,530, 1997

Mahafza, B. R., *Radar Systems Analysis and Design Using MATLAB*, 2^{nd}. Chapman & Hall, 2005

Meikle, H., *Modern Radar Systems*, Artech House, 2001

Mike Kossor, A Broadband HF Amplifier Using Low-cost Power MOSFETs, *ARRL Handbook*, pp.17.87-17.93, 2001

Munro, G. H., Travelling disturbances in the ionosphere, *Proceedings of the Royal Society of London. Series A, Mathematical and Physical Sciences*, Vol. 202, No. 1069, pp. 208-223, July, 1950

Munro, G. H., Reflexions from Irregularities in the Ionosphere, *Proceedings of the Royal Society of London. Series A, Mathematical and Physical Sciences*, Vol. 219, No. 1139, pp. 447-463, October, 1953

Munro, G. H., Traveling ionospheric disturbances in the F region, *Australian Journal of Physics*, vol. 11, pp.91-112, 1958

Rao, K.V., Reddy, V.U., Biphase sequence generation with low sidelobe autocorrelation function, *IEEE Trans. Aerospace and Electronic Systems,* vol. AES-22, no. 2, pp. 128–133, March 1986

Waldock, J. A., Jones, T. B., HF Doppler observations of medium-scale traveling ionospheric disturbances at mid-latitudes, *Journal of Atmospheric and Terrestrial Physics*, vol. 48, pp. 245-260, March 1986

Wang, L., Ionospheric Tomography in the CASSIOPE /e-POP Satellite Mission, Ph.D. thesis, Dept. of Elect. Eng., University of Western Ontario, 2006

Wolfgang, L. D., etc, *The ARRL Handbook for Radio Amateurs 68th*, American Radio Relay League, Newington,1991